Cell Reports

Article

# NGFR regulates stromal cell activation in germinal centers

## Graphical abstract

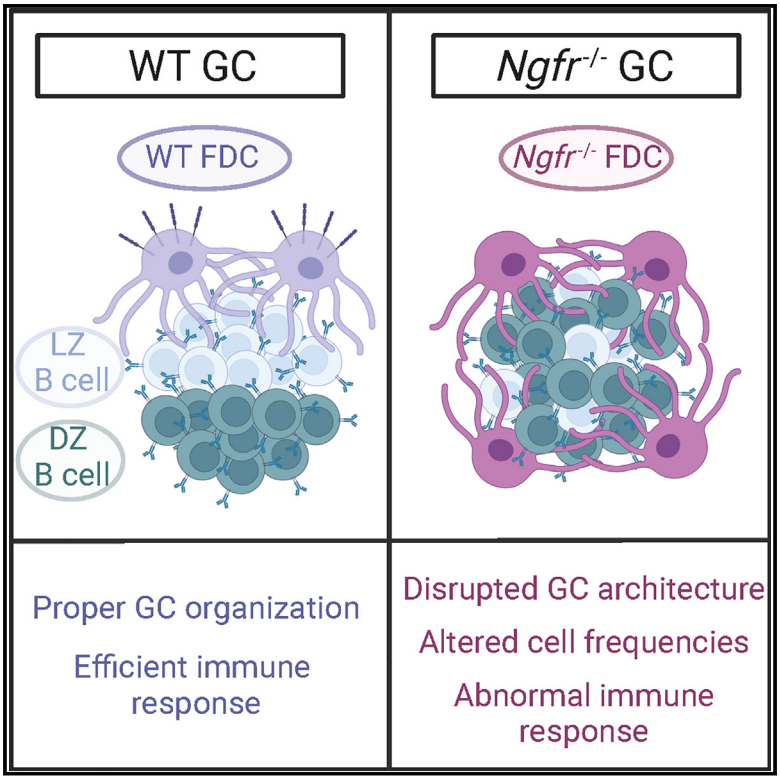


## Highlights

- The nerve growth factor receptor (NGFR) is modulated in FDCs upon GC formation
- NGFR absence in lymphoid stromal cells leads to alterations in GC structure
- *Ngfr*$^{-/-}$ GCs show an aberrant humoral immune response and autoantibody production
- In the context of impaired B cell apoptosis, *Ngfr*$^{-/-}$ enhances autoimmunity development

## Authors

Alberto Hernández-Barranco, Vanesa Santos, Marina S. Mazariegos, ..., Michel Cogne, Karin Tarte, Héctor Peinado

## Correspondence

hpeinado@cnio.es

## In brief

Hernández-Barranco et al. demonstrate the role of NGFR in FDC physiology, regulating humoral immune responses. Depleting NGFR leads to spontaneous germinal center formation, alters stromal cells, and increases autoantibodies. Their findings shed light on the involvement of NGFR in immune tolerance and potential therapeutic avenues.

Hernández-Barranco et al., 2024, Cell Reports ■■, 113705 ■■, 2024 
https://doi.org/10.1016/j.celrep.2024.113705

CellPress

Cell Reports

CellPress
OPEN ACCESS

Article

# NGFR regulates stromal cell activation in germinal centers

Alberto Hernández-Barranco,[1] Vanesa Santos,[1] Marina S. Mazariegos,[1,2] Eduardo Caleiras,[3] Laura Nogués,[1] Frédéric Mourcin,[4] Simon Léonard,[4] Christelle Oblet,[5] Steve Genebrier,[4] Delphine Rossille,[4,6] Alberto Benguría,[7] Alba Sanz,[8] Enrique Vázquez,[7] Ana Dopazo,[7] Alejo Efeyan,[8] Ana Ortega-Molina,[8,9] Michel Cogne,[4] Karin Tarte,[4,6] and Héctor Peinado[1,10,*]

[1]Microenvironment and Metastasis Laboratory, Molecular Oncology Program, Spanish National Cancer Research Center (CNIO), 28029 Madrid, Spain
[2]Liver Injury and Inflammation Laboratory, Department of Immunology, Ophthalmology and ENT, School of Medicine, Complutense University, 28040 Madrid, Spain
[3]Histopathology Unit, Biotechnology Program, Spanish National Cancer Research Center (CNIO), 28029 Madrid, Spain
[4]UMR U1236, University Rennes, INSERM, EFS Bretagne, Equipe Labellisée Ligue Contre le Cancer, 35000 Rennes, France
[5]Immunology Department, Faculty of Medicine, Limoges University, CNRS Umr 7276, Inserm U1262, 87000 Limoges, France
[6]SITI Lab, Pôle Biologie, CHU Rennes, 35000 Rennes, France
[7]Genomic Unit, Spanish National Cardiovascular Research, Carlos III, 28029 Madrid, Spain
[8]Metabolism and Cell Signaling Laboratory, Molecular Oncology Program, Spanish National Cancer Research Centre (CNIO), 28029 Madrid, Spain
[9]Metabolism in Cancer and Ageing Laboratory, Immune System and Function Department, Centro de Biología Molecular "Severo Ochoa" (CMBSO-CSIC), Madrid 28049, Spain
[10]Lead contact
*Correspondence: hpeinado@cnio.es
https://doi.org/10.1016/j.celrep.2024.113705

## SUMMARY

Nerve growth factor receptor (NGFR) is expressed by follicular dendritic cells (FDCs). However, the role of NGFR in the humoral response is not well defined. Here, we study the effect of *Ngfr* loss on lymph node organization and function, demonstrating that *Ngfr* depletion leads to spontaneous germinal center (GC) formation and an expansion of the GC B cell compartment. In accordance with this effect, stromal cells are altered in *Ngfr*$^{-/-}$ mice with a higher frequency of FDCs, characterized by CD21/35, MAdCAM-1, and VCAM-1 overexpression. GCs are located ectopically in *Ngfr*$^{-/-}$ mice, with lost polarization together with impaired high-affinity antibody production and an increase in circulating autoantibodies. We observe higher levels of autoantibodies in *Bcl2* Tg/*Ngfr*$^{-/-}$ mice, concomitant with a higher incidence of autoimmunity and lower overall survival. Our work shows that NGFR is involved in maintaining GC structure and function, participating in GC activation, antibody production, and immune tolerance.

## INTRODUCTION

The nerve growth factor (NGF) receptor (NGFR), also known as p75$^{NTR}$, belongs to the tumor necrosis factor receptor superfamily. NGFR is a low-affinity receptor of neurotrophins including NGF,[1] brain-derived neurotrophic factor (BDNF),[2] and neurotrophin-3, -4, and -5.[3,4,5] NGFR was discovered in the nervous system controlling cell survival and apoptosis,[6–8] but it was later described in other organs fulfilling a variety of roles in different processes.[9,10]

Follicular dendritic cells (FDCs) express NGFR,[11,12] being involved in FDC maintenance,[13] although its functional role in FDCs remains poorly explored. FDCs are a subset of lymphoid stromal cells (LSCs)[14–17] involved in controlling B cell maturation and selection within germinal centers (GCs).[18,19] The microstructural organization of GCs ensures their correct functioning, being regulated by the genetic program of B lymphocytes and by paracrine signals.[20,21] In fact, alterations to the microenvironment affect conditions such as autoimmunity and follicular lymphoma.[21–24]

Here, we analyzed the role of NGFR in lymph nodes (LNs) and the implications of its loss in autoimmunity. We found that NGFR expression is modulated upon FDC activation by immunization, and we characterized the phenotype of secondary lymphoid organs (SLOs) in a *Ngfr*$^{-/-}$ mouse model. These mice had enlarged LNs due to GC hyperplasia and spontaneous activation, alterations that were reproduced when *Ngfr* was depleted in the non-hematopoietic compartment. The GCs in *Ngfr*$^{-/-}$ LNs have structural and functional abnormalities when compared to GCs induced by immunization in wild-type (WT) mice. These alterations included ectopic GC location, a loss of dark zone/light zone (DZ/LZ) polarization, impaired high-affinity antibody production, and the presence of circulating autoantibodies. FDCs were the main LSC population increased in the LNs of naive *Ngfr*$^{-/-}$ mice with overexpression of CD21/35, MAdCAM-1, and VCAM-1. To

Please cite this article in press as: Hernández-Barranco et al., NGFR regulates stromal cell activation in germinal centers, Cell Reports (2024), https://doi.org/10.1016/j.celrep.2024.113705



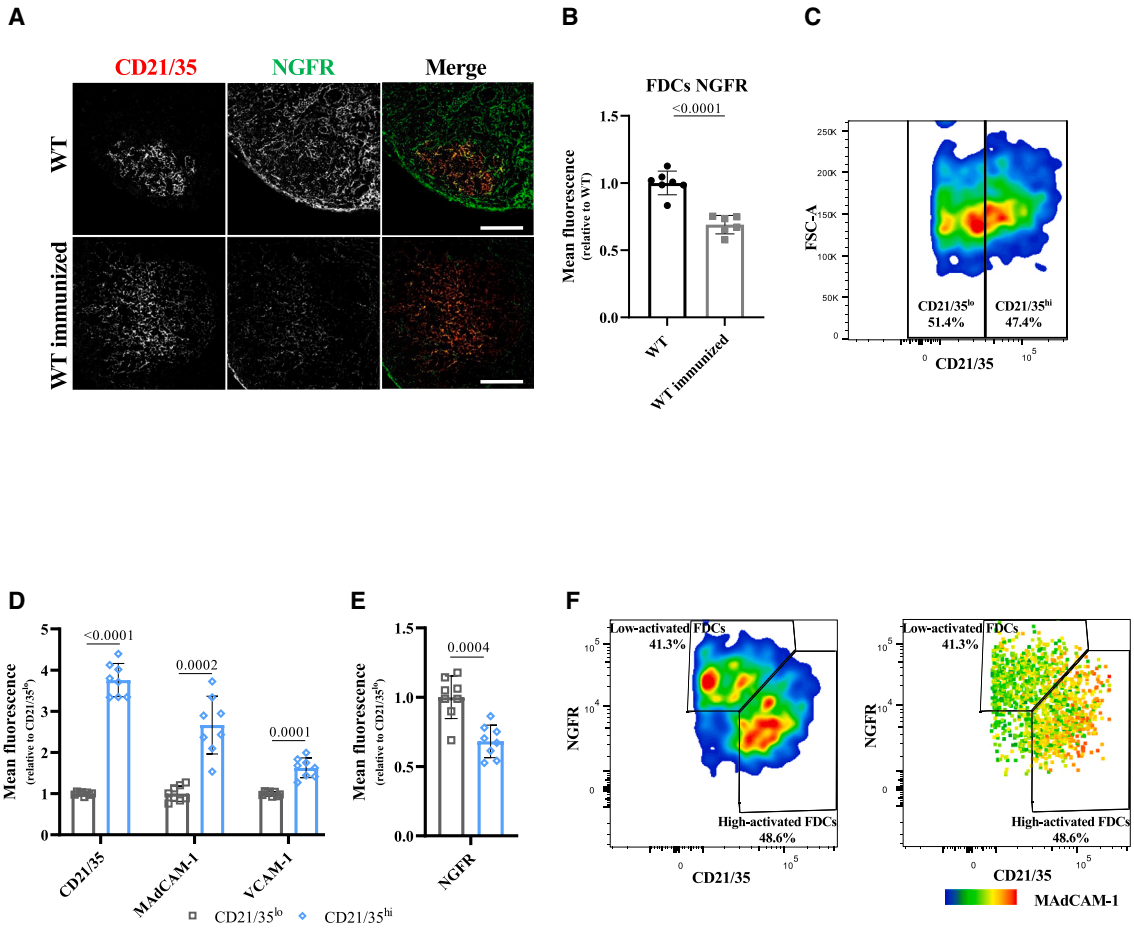


**Figure 1. NGFR is modulated in FDCs by immunization**

(A) Representative IHF images of CD21/35 (red) and NGFR (green) in GCs from WT or WT immunized PO LNs. Scale bar, 100 μm.

(B) Quantification of the mean NGFR fluorescence in FDCs (CD21/35$^+$) from WT or WT immunized PO LNs (n = 7 WT and 6 WT immunized LNs from 1 experiment).

(C) Gating strategy used to select the CD21/35$^{hi}$ and CD21/35$^{lo}$ populations among the PO LN FDCs 10 days after immunization of WT mice.

(D) Flow cytometry mean fluorescence quantification of the markers of FDC activation in the populations gated in (C).

(E) Flow cytometry quantification of the mean NGFR fluorescence in the populations gated in (C) (n = 8 from 2 independent experiments for D and E).

(F) Representative pseudocolor plot (left panel) and heatmap statistics plot (right panel) of immunized FDCs, the latter showing the mean MAdCAM-1 fluorescence. The representative plots in (C) and (F) were generated by file concatenation of the gated FDCs in 4 biological replicates. The graphs in (B), (D), and (E) show the mean and SD error bars and the p values by two-tailed unpaired t test with Welch's correction.

gain better insight into the regulation of autoimmunity, we depleted *Ngfr* in a *Bcl2* transgenic (Tg) mouse model.[25] Double-mutant mice had more autoantibodies in serum and a higher incidence of lupus-like glomerulonephritis with lower overall survival (OS). Our work shows that NGFR regulates GC activation and B cell immune responses by preserving peripheral tolerance and preventing autoimmunity.

## RESULTS

### NGFR is modulated in FDCs by immunization

We first studied NGFR expression in FDCs during an immune response after immunization of WT mice. We injected 4-hydroxy-3-nitrophenyl-acetyl (NP) hapten conjugated to keyhole limpet hemocyanin (NP-KLH) by subcutaneous footpad injection,[26] and the expression of NGFR in CD21/35$^+$ FDCs was analyzed by immunohistofluorescence (IHF). NGFR expression fell significantly in FDCs 10 days post immunization (Figures 1A and 1B). We used CD21/35 expression to differentiate FDC activation[27,28] in LNs from immunized WT mice by flow cytometry. Other markers of LZ-FDC activation were also enhanced in CD21/35$^{hi}$ FDCs such as MAdCAM-1 and VCAM-1 (Figures 1C and 1D). We then analyzed the expression of NGFR in these populations and found that it was less expressed by CD21/35$^{hi}$ FDCs (Figure 1E). Hence, NGFR modulation appears to be correlated with FDC activation and differentiation, exhibiting an inverse correlation with the other markers of LZ-FDC activation (Figure 1F).

### Spontaneous germinal center formation in *Ngfr*$^{-/-}$ mice

To further explore the role of NGFR in this context, we characterized the SLOs in *Ngfr*$^{-/-}$ mice,[29] assessing the anatomy of their LNs. *Ngfr*$^{-/-}$ LNs were significantly larger, particularly popliteal

Please cite this article in press as: Hernández-Barranco et al., NGFR regulates stromal cell activation in germinal centers, Cell Reports (2024), https://doi.org/10.1016/j.celrep.2024.113705



CellPress
OPEN ACCESS

(PO) LNs (Figure 2A), increasing their weight approximately 5-fold compared to WT (Figure 2B), as well as in brachial (BR) LNs (Figures S1A and S1B). We compared the distribution of CD45R/B220, Ki67, and BCL6 in LNs from WT and *Ngfr*$^{-/-}$ mice by immunohistochemistry (IHC) staining. Based on the expression of CD45R/B220$^{+}$, *Ngfr*$^{-/-}$ mice exhibited substantial hyperplasia in the B cell compartment (Figure 2C). Moreover, the BCL6$^{+}$ staining of the GCs in *Ngfr*$^{-/-}$ in PO LNs (Figure 2C) and BR LNs (Figure S1C) coincided with staining for the Ki67 marker of proliferation, as opposed to that in WT mice (Figure 2C).

A flow cytometry analysis of B cells in the LNs (Figure 2D) confirmed the increase of the total CD19$^{+}$ B cell compartment in *Ngfr*$^{-/-}$ relative to WT in PO LNs (Figures 2D and 2E) and BR LNs (Figure S1D). Furthermore, the proportion of CD19$^{+}$ CD95$^{+}$CD38$^{lo}$ GC B cells increased significantly in both PO LNs (Figures 2D and 2F) and BR LNs (Figure S1E). These differences were also observed when the total number of cells/LN was analyzed in both PO (Figures S1F and S1G) and BR LNs (Figures S1H and S1I). Together, these data demonstrate that the loss of NGFR is sufficient to trigger spontaneous B cell activation in the GCs of LNs.

## FDCs are the main population altered in *Ngfr*$^{-/-}$ mice

To explore the possible implication of NGFR in early B cell development, we analyzed NGFR expression at different stages of bone marrow (BM) B cell precursor maturation (Pro-B cells, Pre-BI cells, Pre-BII cells, and immature B cells[30]: Figure S2A). On average, we found that there were fewer than 3% NGFR$^{hi}$ cells in each subset, and only immature B cells exhibited a slight shift in NGFR mean fluorescence (Figures S2B and S2C). Notably, no imbalance was found in any of those populations when *Ngfr* WT and *Ngfr*$^{-/-}$ BM was compared (Figure S2D). Flow cytometry analysis revealed no or weak NGFR expression in the majority of B cells (CD19$^{+}$) in WT immunized LNs, with a shift in NGFR fluorescence relative to *Ngfr*$^{-/-}$ B cells similar to that evident in immature B cells in the BM (Figures S2E and S2F, upper panels). Nonetheless, a small subpopulation of approximately 20% of the CD19$^{+}$CD95$^{+}$CD38$^{lo}$ GC B cells expressed low levels of NGFR (Figures S2E and S2F, lower panels).

To understand if the lack of NGFR in GC B cells was responsible for the LN hyperplasia in *Ngfr*$^{-/-}$ mice, BM transplantation experiments were performed on sub-lethally irradiated WT and *Ngfr*$^{-/-}$ recipient mice, using donor BM cells from WT and *Ngfr*$^{-/-}$ mice (Figure 3A). LN enlargement was independent of the BM origin and only occurred in *Ngfr*$^{-/-}$ transplanted hosts (Figure 3B). Indeed, flow cytometry analysis confirmed that the B cell compartment only expanded significantly in *Ngfr*$^{-/-}$ hosts irrespective of the BM origin (Figure 3C). While WT hosts had barely detectable GC B cells (less than 0.2% of all LN B cells), the GC B cells in *Ngfr*$^{-/-}$ hosts represented about 4%–5% of the CD19$^{+}$ B cell population (Figure 3D). To rule out the influence of *Ngfr*$^{-/-}$ in BM cell engraftment, we analyzed the percentage of chimerism after BM transplantation in WT and *Ngfr*$^{-/-}$ hosts using a hematopoietic cell tracking system based on the allelic variants CD45.1 and CD45.2. We observed that the total BM cell replacement was around 85% (Figure S2G) and over 95% for B cells (B220$^{+}$ cells) (Figure S2H). Of note, no differences were found regardless of the *Ngfr* status in the donor BM, suggesting the involvement of non-hematopoietic cell populations in the phenotype observed.

To identify the non-hematopoietic cell subsets affected by *Ngfr*$^{-/-}$, we characterized NGFR expression in LN cells from WT mice. Most NGFR-expressing cells were elongated and interconnected, mainly confined to the cortical and B cell areas (Figure S3A). Flow cytometry analysis showed that NGFR was expressed in approximately 50% of non-hematopoietic CD45$^{-}$ cells and in only 0.5% of the CD45$^{+}$ hematopoietic cells (Figure S3B). Moreover, an analysis of the CD45$^{-}$ cell subsets (Figure S3C) highlighted the weak NGFR expression by CD31$^{+}$podoplanin (PDPN)$^{+}$ lymphatic endothelial cells (LECs) and its strong expression by the 3 main PDPN$^{+}$ LSC subsets, including MAdCAM-1$^{-}$CD21/35$^{-}$ fibroreticular cells (FRCs), MAdCAM-1$^{+}$CD21/35$^{-}$ marginal reticular cells (MRCs), and CD21/35$^{+}$ FDCs (Figures 3E and S3D).

When the effect of *Ngfr*$^{-/-}$ on LN LSC populations was studied in naive mice, there was an enrichment of total non-hematopoietic CD45$^{-}$ cells in *Ngfr*$^{-/-}$ mice (Figure S3E). We applied a dimensionality reduction approach, based on the uniform manifold approximation and projection (UMAP),[31] to our flow cytometry data from WT and *Ngfr*$^{-/-}$ stromal cells (SCs), and the main population altered in *Ngfr*$^{-/-}$ mice corresponded to FDCs based on the expression of the canonical FDC marker CD21/35 (Figure 3F, red square). We next quantified the populations of cells affected in *Ngfr*$^{-/-}$ mice LNs; while blood endothelial cells (BECs), LECs, and CD31$^{-}$PDPN$^{-}$ double-negative cells were not affected in *Ngfr*$^{-/-}$ mice, FRCs, MRCs, and FDCs expanded significantly (Figure 3G). Overall, these data indicate that *Ngfr*$^{-/-}$ mainly affects the LN LSC compartment, leading to an expansion of LSCs and, particularly, FDCs.

## NGFR deficiency promotes FDC activation and upregulates B cell-activating signatures

Given that FDCs were the most significantly expanded stromal population in *Ngfr*$^{-/-}$ LNs, and taking into account their well-established roles in GC physiology,[15,16,19] we wondered whether FDC activation might also be affected in *Ngfr*$^{-/-}$ mice, contributing to B cell expansion. We performed RNA sequencing (RNA-seq) experiments on sorted CD45$^{-}$CD31$^{-}$PDPN$^{+}$CD21/CD35$^{+}$ LN FDCs from naive WT and *Ngfr*$^{-/-}$ mice using SMART-Seq RNA-seq technology. A principal component analysis (PCA) showed that the samples clustered based on their NGFR status (Figure 4A) such that we could identify differentially expressed genes (DEGs) between the WT and *Ngfr*$^{-/-}$ cells. We found 290 significantly upregulated genes and 157 downregulated genes in *Ngfr*$^{-/-}$ FDCs relative to their WT counterparts (Figure 4B and Table S1). A gene set enrichment analysis (GSEA) using the Reactome database revealed enrichment in *Ngfr*$^{-/-}$ FDCs for the adaptive immune system and for cytokine signaling in the immune system among others (Figure 4C and Table S2). Indeed, genes involved in the modulation of the GC reaction, like *Fcer2*, *Tnfrsf9*, *Madcam1*, *Cd40*, *Il4r*, *Vcam1*, or *Cd80*, were all upregulated in *Ngfr*$^{-/-}$ FDCs (Table S1).

The FDC signature of *Ngfr*$^{-/-}$ FDCs (Table S1) was compared with previously published single cell RNA-seq (scRNA-seq) datasets from specific subsets of murine LSCs.[27,32] An initial comparison with data from whole purified non-endothelial LN SCs

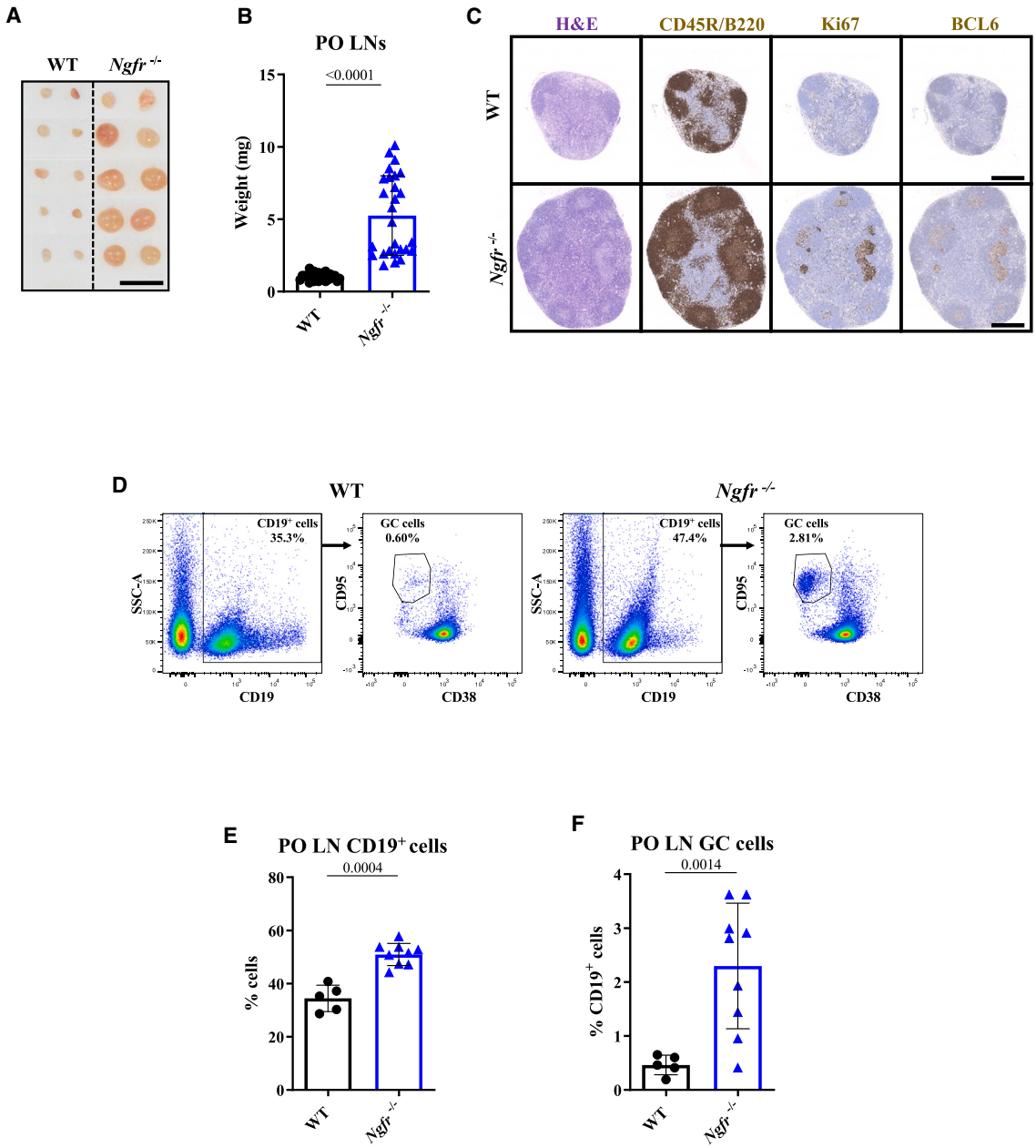


**Figure 2. The absence of NGFR in the LN microenvironment leads to GC hyperplasia in *Ngfr*$^{-/-}$ mice**

(A) Representative image of the PO LN size in WT and *Ngfr*$^{-/-}$ mice. Scale bar, 5 mm.

(B) PO LN weight in WT and *Ngfr*$^{-/-}$ mice (n = 28 from 3 independent experiments).

(C) Representative H&E staining and immunohistochemistry for CD45R/B220, Ki67, and BCL6 in PO LNs of WT (upper panels) and *Ngfr*$^{-/-}$ (lower panels). Scale bar, 400 μm.

(D) Gating strategy for CD19$^{+}$ and GC cells and representative samples of PO LN from WT (left panels) and *Ngfr*$^{-/-}$ (right panels) mice.

(E) Flow cytometry quantification of PO LN CD19$^{+}$ cells in WT and *Ngfr*$^{-/-}$ mice (n = 5 from 1 experiment for WT, and n = 9 from 2 independent experiments on *Ngfr*$^{-/-}$ mice).

(F) Flow cytometry quantification of PO LN GC cells in WT and *Ngfr*$^{-/-}$ mice (n = 5 from 1 experiment for WT, and n = 9 from 2 independent experiments on *Ngfr*$^{-/-}$ mice). The graphs show the mean SD and error bars. For (B), the p values by a two-tailed Mann-Whitney test and by a two-tailed unpaired t test with Welch's correction in (E) and (F).

Please cite this article in press as: Hernández-Barranco et al., NGFR regulates stromal cell activation in germinal centers, Cell Reports (2024), https://doi.org/10.1016/j.celrep.2024.113705



CellPress
OPEN ACCESS

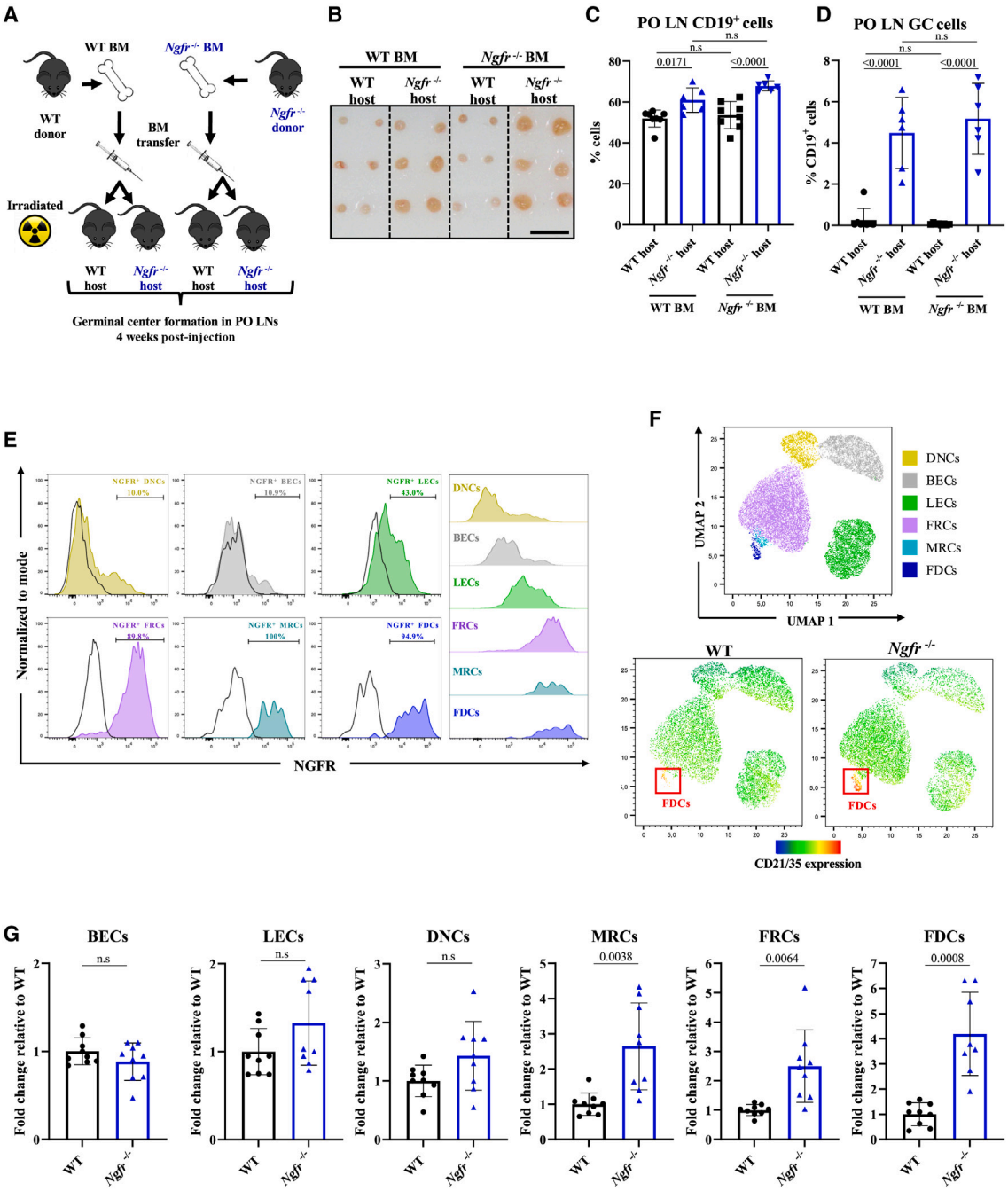


**Figure 3. GC hyperplasia is driven by *Ngfr*$^{-/-}$ stromal cells and FDCs are the main population altered**

(A) Experimental setup for BM transfer to irradiated WT and *Ngfr*$^{-/-}$ mice.

(B) Representative PO LN sizes in irradiated WT and *Ngfr*$^{-/-}$ mice 4 weeks after BM transplant as indicated in (A). Scale bar, 5 mm.

(C) Flow cytometry quantification of PO LN CD19$^{+}$ cells in WT and *Ngfr*$^{-/-}$ irradiated mice, as indicated in (A) (n = 8 from 2 independent experiments for WT host, and n = 6 from 2 independent experiments for *Ngfr*$^{-/-}$ host mice).

(D) Flow cytometry quantification of PO LN GC cells in WT and *Ngfr*$^{-/-}$ irradiated mice as indicated in (A) (n = 8 from 2 independent experiments for WT host, and n = 6 from 2 independent experiments for *Ngfr*$^{-/-}$ host mice).

(E) Histograms comparing NGFR fluorescence in stromal populations of WT LNs. The black lines represent NGFR fluorescence in *Ngfr*$^{-/-}$ SCs used as negative control.

*(legend continued on next page)*

Please cite this article in press as: Hernández-Barranco et al., NGFR regulates stromal cell activation in germinal centers, Cell Reports (2024), https://doi.org/10.1016/j.celrep.2024.113705



showed that upregulated genes in the *Ngfr*$^{-/-}$ FDCs were significantly enriched the FDC subset identified in this work[32] (Figures S4A, S4B, and S4C). In addition, we analyzed the heatmaps generated comparing the top 10 DEGs defining the 9 different subsets identified in this study.[32] We found that the top 10 genes defining the FDC subset (including *Cr2*, *Fcgr2b*, or *Fcer2a*)[32] were all upregulated in *Ngfr*$^{-/-}$ FDCs (Figure S4D). We then compared our signature with that from a published scRNA-seq dataset restricted to mouse B cell-interacting SCs identified as CXCL13-expressing cells in LNs.[27] Among the 7 distinct SC subsets identified previously,[27] the genes upregulated in *Ngfr*$^{-/-}$ FDCs were enriched in the FDC1 cluster, corresponding to LZ-FDCs rather than the DZ-FDC, MRC, or FRC subsets (Figures S3E, S3F, and S3G). Moreover, we studied the correlation between our *Ngfr*$^{-/-}$ FDC gene signature and the genes induced in LZ-FDCs upon immunization. Interestingly, the genes upregulated in FDCs from our *Ngfr*$^{-/-}$ mice were enriched in LZ-FDCs from immunized rather than naive WT mice,[27] as denoted by the higher values of the *Ngfr*$^{-/-}$ upregulated genes' signature and lower values of the *Ngfr*$^{-/-}$ downregulated genes' signature respectively shown in the violin plots (Figure 4D). We extracted the 174 DEGs between naive and immunized LZ-FDCs,[27] obtaining 84 upregulated and 90 downregulated genes (Table S3). Indeed, a GSEA showed that the genes upregulated upon immunization correlated with the most strongly upregulated genes in *Ngfr*$^{-/-}$ FDCs, while the opposite results were obtained with the downregulated signature (Figure 4E).

We generated a curated list of genes gathering those FDC markers modulated in the *Ngfr*$^{-/-}$ FDCs that were also modulated upon inflammation in WT FDCs (Figure 4F and Table S4). We validated that CD21/35, MAdCAM-1, and VCAM-1 were also upregulated at the protein level by flow cytometry in *Ngfr*$^{-/-}$ FDCs relative to WT FDCs (Figures 4G, 4H, and 4I). Moreover, the expressions of MAdCAM-1 (Figure 4J) and VCAM-1 (Figure 4L) were upregulated about 3- and 1.4-fold, respectively, in CD21/35$^{+}$ cells *in situ* by IHF (Figures 4K and 4M). Overall, these data show that the CD21/35$^{+}$ LSCs in naive *Ngfr*$^{-/-}$ mice adopt an activated phenotype with similar transcriptomic and phenotypic profiles to LZ-FDCs in immunized mice.

## GC structure and function is aberrant in *Ngfr*$^{-/-}$ mice

We compared GC formation in immunized WT mice and naive *Ngfr*$^{-/-}$ mice. BCL6 and CD21/CD35 expression indicated that GC localization within the LN might be aberrant in *Ngfr*$^{-/-}$ mice, since these microstructures were not only found in the cortical area but also in the medulla, suggesting ectopic GC formation in the LNs of *Ngfr*$^{-/-}$ mice (Figure 5A). The studies of GC structure identified major alterations in *Ngfr*$^{-/-}$ mice. H&E staining highlighted classic LZ/DZ areas within the GC of immunized WT mice, whereas such organization was disrupted in most GCs of *Ngfr*$^{-/-}$ mice, which displayed a more homogeneous histological appearance similar to the DZ area (Figure 5B, upper panels). Since FDCs are fundamental organizers of GC structure, we analyzed CD21/35 expression (Figure 5B, lower panels), observing a typical distribution of CD21/35$^{+}$ cells in the LZ of GCs from immunized WT mice. Conversely, CD21/35$^{+}$ cells were distributed homogenously in the GCs of naive *Ngfr*$^{-/-}$ mice with no apparent regionalization (Figure 5B, lower panels). Importantly, both features were maintained in *Ngfr*$^{-/-}$ upon immunization, indicating that immunization does not rescue GC compartmentalization in knockout mice (Figures S5A and S5B). To further characterize the GCs in *Ngfr*$^{-/-}$ mice, we studied GC B cell proliferation through Ki67 staining. Proliferation was mainly restricted to the CD21/35$^{-}$ DZ area of GCs in WT immunized mice, while it was more homogeneous in the GCs from *Ngfr*$^{-/-}$ mice (Figure 5C). We next analyzed by flow cytometry, the frequency of LZ and DZ B cells in the LNs of immunized WT, naive *Ngfr*$^{-/-}$, and immunized *Ngfr*$^{-/-}$ mice based on the expression of the CD86 and CXCR4 markers[33] (Figure 5D). The DZ/LZ B cell ratio increased significantly in *Ngfr*$^{-/-}$ mice relative to immunized WT mice (Figure 5E). Importantly, after immunization, *Ngfr*$^{-/-}$ mice did not display differences compared to non-immunized *Ngfr*$^{-/-}$ mice (Figure 5E), suggesting that immunization of *Ngfr*$^{-/-}$ does not result in a correction of the GC structure or polarization. These data confirm that despite being surrounded by LZ-like FDCs, GC B cells are skewed toward a DZ phenotype in *Ngfr*$^{-/-}$ mice.

We evaluated whether the abnormalities observed in *Ngfr*$^{-/-}$ mice affected the generation of high-affinity antibodies (Figure 5F). As such, we immunized WT and *Ngfr*$^{-/-}$ mice by subcutaneous injection of NP-KLH into the footpad (day 0), and we analyzed the generation of low- (Figure 5G) and high-affinity (Figure 5H) IgG1 antibodies against NP every 7 days for 4 weeks post immunization. To analyze these differences, we normalized antibody levels to the initial titers measured on day 7, and we found that the production of both types of antibodies increased significantly over time in WT mice. By day 28, there was a 2.36- and 88.66-fold increase for low- and high-affinity antibodies, respectively, in the WT compared to the *Ngfr*$^{-/-}$ mice (Figures 5G and 5H). We established the ratio between high- and low-affinity antibody levels to evaluate the effectiveness of high-affinity antibody production during the humoral immune response.[26] We found that this ratio was significantly higher in the WT than in the *Ngfr*$^{-/-}$ mice (Figure 5I), suggesting that the efficiency of the high-affinity humoral response is compromised over time in the *Ngfr*$^{-/-}$ mice.

Due to the pivotal role of T follicular (Tf) cells in selection of high-affinity B cell clones, we assessed if this population was altered in the *Ngfr*$^{-/-}$ GCs. Flow cytometry analysis (see Figure S5C for gating strategy) showed no alterations in T cell (CD3$^{+}$), CD4$^{+}$, and CD4$^{-}$ T cell populations in the LNs of *Ngfr*$^{-/-}$ relative to WT immunized mice (Figures S5D, S5E, and S5F). Although the total

(F) UMAP of the stromal populations gated in Figure S3C (upper panel) in which an equal number of CD45$^{-}$ events from 5 WT to 5 *Ngfr*$^{-/-}$ samples were merged. The lower panels show the intensity distribution of CD21/35 in the UMAP separating WT and *Ngfr*$^{-/-}$ events.

(G) Flow cytometry analysis of the different subsets of stromal populations gated in Figure S3C. The frequency of the total cells relative to the WT values is expressed as the fold change for each population (n = 9 from 2 independent experiments; one outlier was removed from *Ngfr*$^{-/-}$ FDCs). The graphs show the mean and SD error bars. For (C) and (D), the p values are by one-way ANOVA analysis and Tukey's multiple comparisons test, and a two-tailed unpaired t test with Welch's correction was used in (G) (except in LECs, where a Mann-Whitney test was used).

Please cite this article in press as: Hernández-Barranco et al., NGFR regulates stromal cell activation in germinal centers, Cell Reports (2024), https://doi.org/10.1016/j.celrep.2024.113705



CellPress
OPEN ACCESS

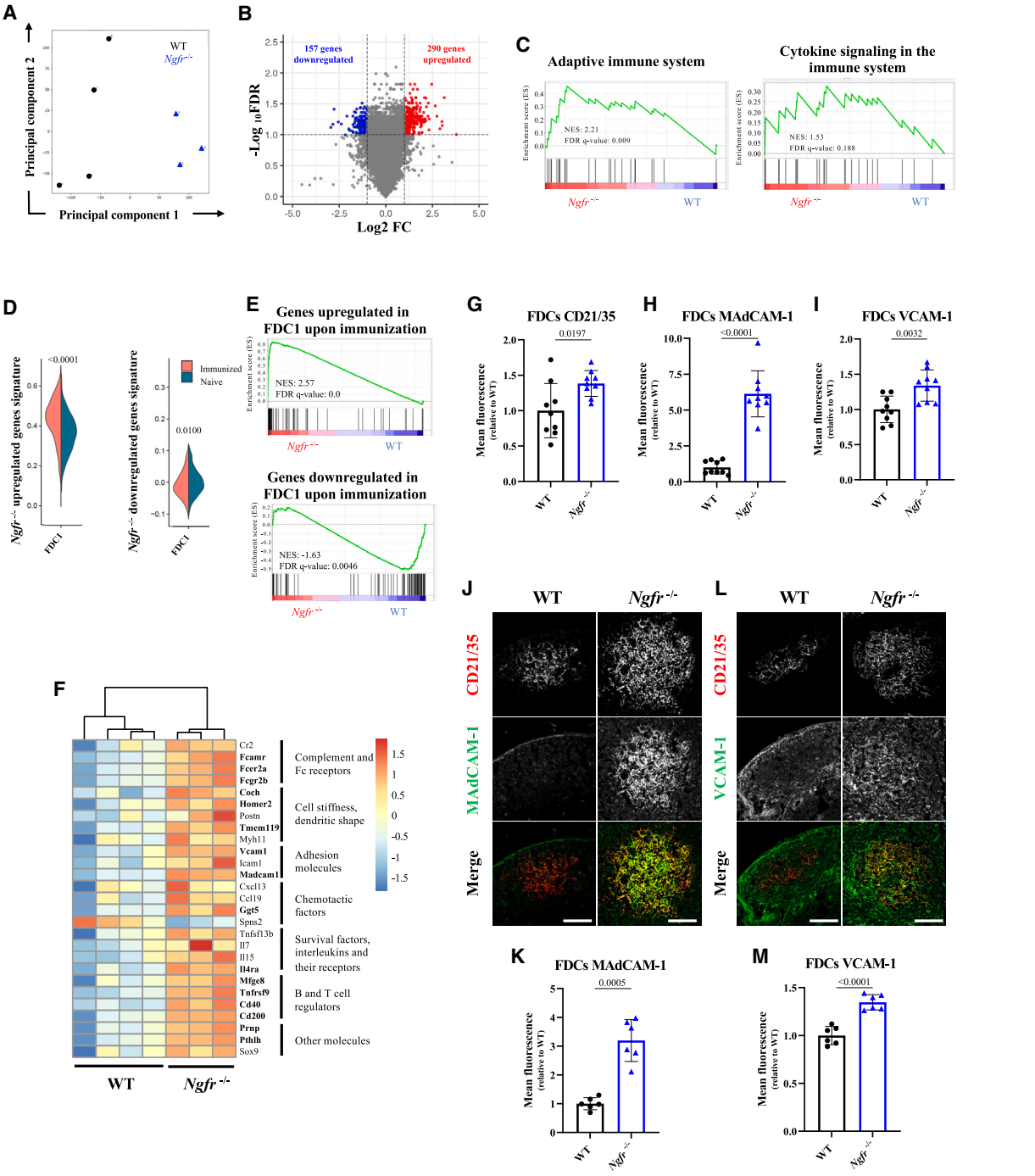


**Figure 4. NGFR deficiency upregulates B cell-activating signatures**

(A) A principal component analysis (PCA) of the samples evaluated in the RNA-seq analysis (n = 4 for WT and n = 3 for *Ngfr*$^{-/-}$ mice).

(B) A volcano plot showing the gene distribution upon a differential expression analysis on *Ngfr*$^{-/-}$ and WT mice. The colored dots represent genes with an FDR <0.1 and FC >1 (red) or <–1 (blue): see STAR Methods for more details.

(C) Enrichment plot from the Reactome adaptive immune system signature (left panel) and cytokine signaling in the immune system (right panel) upon GSEA with the DEGs obtained from the RNA-seq analysis in FDCs.

(D) Violin plots showing the relative identity of the DEG signatures in the FDCs from *Ngfr*$^{-/-}$ and WT mice and compared with the FDC1 (LZ-FDCs) subset found by Pikor NB et al.[27] in immunized (orange) and naive (green) LNs.

(E) Enrichment plots of GSEA of the DEGs between FDC1 immunized and naive LNs in Pikor NB et al.[27] compared to the DEG signatures in FDCs from *Ngfr*$^{-/-}$ and WT mice.

*(legend continued on next page)*

Please cite this article in press as: Hernández-Barranco et al., NGFR regulates stromal cell activation in germinal centers, Cell Reports (2024), https://doi.org/10.1016/j.celrep.2024.113705



Tf cells ($CD3^+CD4^+CXCR5^+PD\text{-}1^+$) remain unaltered (Figure 5J), we analyzed the ratio between the Tf helper (Tfh) cells ($CD3^+CD4^+CXCR5^+PD\text{-}1^+FOXP3^-$) and the Tf regulatory (Tfr) cells ($CD3^+CD4^+CXCR5^+PD\text{-}1^+FOXP3^+$). Importantly, we found a significant increase of Tfh cells (Figure 5K) and a decrease in the Tfr populations in *Ngfr*$^{-/-}$ LNs (Figure 5L).

### *Ngfr*$^{-/-}$ boosts the pathological phenotypes and decreases survival by enhancing autoimmunity in the context of BCL2 overexpression

Since the activation of GCs without appropriate B cell selection has been directly linked to the appearance of autoreactive clones,[22] we evaluated the effect of *Ngfr*$^{-/-}$ on autoimmunity. We assessed the presence of IgG anti-nuclear antibodies (ANAs) in the serum of 10-week-old WT and *Ngfr*$^{-/-}$ mice, detecting IgG ANAs at dilutions of 1/50, 1/250, and 1/500 in *Ngfr*$^{-/-}$ serum (Figures S5G and S5H). By contrast, reactivity was not detected in the serum from control WT mice tested at any dilution. We also evaluated whether the autoantibodies in *Ngfr*$^{-/-}$ mice could contribute to the development of autoimmune diseases in aged animals by following a cohort of 7 WT and 13 *Ngfr*$^{-/-}$ mice for up to 85 weeks. No clinical signs, increased mortality, or autoimmune damage in the organs was evident in these mice. Hence, we further studied this phenotype in a context more prone to the development of autoimmune lesions.

We crossed *Ngfr*$^{-/-}$ mice with a transgenic mouse overexpressing the antiapoptotic human gene *BCL2* under the control of Vav gene regulatory (VavP) sequences (abbreviated as *Bcl2* Tg).[34] This mouse model has been used previously to evaluate autoimmune diseases *in vivo*.[35,36] When the formation of GCs was studied in 10-week-old mice, the LNs from *Bcl2* Tg/*Ngfr*$^{-/-}$ mice were larger than those of the *Bcl2* Tg/*Ngfr* WT mice, with enhanced BCL6 expression evident by IHC (Figure S6A). Flow cytometry (see Figure S6B for gating strategy) confirmed that there were more GC B cells in *Bcl2* Tg/*Ngfr*$^{-/-}$ PO and BR LNs compared to their WT controls (Figures S6C and S6D), together with an increase in FDC frequency (Figures S6E and S6F). We further analyzed the *Bcl2* Tg/*Ngfr*$^{-/-}$ model at later stages. We studied a cohort of *Bcl2* Tg/*Ngfr*$^{-/-}$ and WT mice at 35 weeks of age, analyzing the histology of their kidneys to define any pathological alterations.[34] The proportion of glomeruli affected by crescent formation due to Bowman's capsule epithelium hyperplasia (a sign of advanced kidney affectation), or the generation of eosinophilic deposits within the glomeruli (typically found when these animals are affected by autoimmunity and related to immunoglobulin accumulation),[35,36] was quantified (Figures 6A and 6B). A significantly higher proportion of glomeruli were affected by Bowman's capsule epithelium hyperplasia (Figure 6C) and eosinophilic deposits (Figure 6D) in the *Bcl2* Tg/*Ngfr*$^{-/-}$ mice than in the *Bcl2* Tg/*Ngfr* WT mice (Figures 6C and 6D), suggesting that *Ngfr*$^{-/-}$ can accelerate the appearance of autoimmune disorders. We also assessed the circulating ANAs in these 35-week-old animals and detected significantly higher ANA titers in the sera of *Bcl2* Tg/*Ngfr*$^{-/-}$ mice than in the *Bcl2* Tg/*Ngfr* WT mice, with most samples exhibiting homogeneous nuclear staining even at the highest dilution tested (1/1,500, Figures 6E and 6F).

To further evaluate whether *Ngfr*$^{-/-}$ might increase the incidence of severe autoimmune phenotypes, we studied the long-term evolution of this pathology in *Bcl2* Tg/*Ngfr*$^{-/-}$ mice and their OS. We found *Bcl2* Tg/*Ngfr*$^{-/-}$ mice had a significantly lower median survival of 231 days as opposed to the 394.5 days in the *Bcl2* Tg/*Ngfr* WT mice (Figure 6G). Macroscopic hemorrhagic foci and a loss of color were evident in the kidneys of most of these mice that died prematurely (Figure 6H), suggesting severe kidney damage. When Bowman's epithelium hyperplasia and the presence of eosinophilic deposits were assessed, the majority of the *Bcl2* Tg/*Ngfr*$^{-/-}$ mice experienced severe kidney damage with more than 30% of their glomeruli affected by either or both phenomena, while less severe kidney lesions were evident in *Bcl2* Tg/*Ngfr* WT mice (Figures 6I and 6J). Notably, the kidney phenotype in the *Bcl2* Tg/*Ngfr* WT mice was predominantly mild or moderate in the mice still alive after 35 weeks relative to those that died before 35 weeks of age (approximately 20% of the cohort).

We established the presence of eosinophilic deposits in more than 20% of the glomeruli as a criterion to stratify mice affected by autoimmunity at the endpoint. Accordingly, we found that 30% of the *Bcl2* Tg/*Ngfr* WT mice died with signs of autoimmunity as opposed to more than 80% of the *Bcl2* Tg/*Ngfr*$^{-/-}$ animals (Figure 6K).

## DISCUSSION

Although NGFR is known to be expressed in immune cells and lymphoid organs,[37] how it participates in the regulation of LN function remains unclear. Here, we analyzed the role of NGFR in LNs using an *Ngfr*$^{-/-}$ mouse model, highlighting the hyperplasia in these LNs in association with an expansion of the GC B cell compartment. Our findings align with previous studies indicating that NGFR expression in most murine B cells remains low but that it is upregulated in antibody-secreting plasma cells of lupus-prone mice.[38] Notably, *Ngfr*$^{-/-}$ in B cells attenuates autoimmune disease progression and negatively affects the generation of B cells in the spleen. Importantly, our BM chimera experiments

(F) Heatmap showing differential expression in FDCs from the RNA-seq analysis of *Ngfr*$^{-/-}$ and WT mice for a selection of the main genes involved in FDC biology. The color coding shows the relative expression standardized by line, and the genes in bold are among the DEGs found when comparing the FDCs from *Ngfr*$^{-/-}$ and WT mice (Table S1).

(G–I) Flow cytometry quantification of the mean (G) CD21/35, (H) MAdCAM-1, and (I) VCAM-1 fluorescence in FDCs from WT and *Ngfr*$^{-/-}$ PO LNs (n = 9 from 2 independent experiments).

(J and L) Representative images from the IHF analysis of CD21/35 (red), (J) MAdCAM-1 (green), and (L) VCAM-1 (green) in WT and *Ngfr*$^{-/-}$ FDCs. Scale bar, 100 μm.

(K and M) Quantification of the mean (K) MAdCAM-1 and (M) VCAM-1 fluorescence in FDCs ($CD21/35^+$) from WT and *Ngfr*$^{-/-}$ PO LNs (n = 6 from 1 experiment). The graphs show the mean and SD error bars and the p values in (D), (G), (H), (I), (K), and (M) by two-tailed unpaired t test with Welch's correction.

Please cite this article in press as: Hernández-Barranco et al., NGFR regulates stromal cell activation in germinal centers, Cell Reports (2024), https://doi.org/10.1016/j.celrep.2024.113705



CellPress
OPEN ACCESS

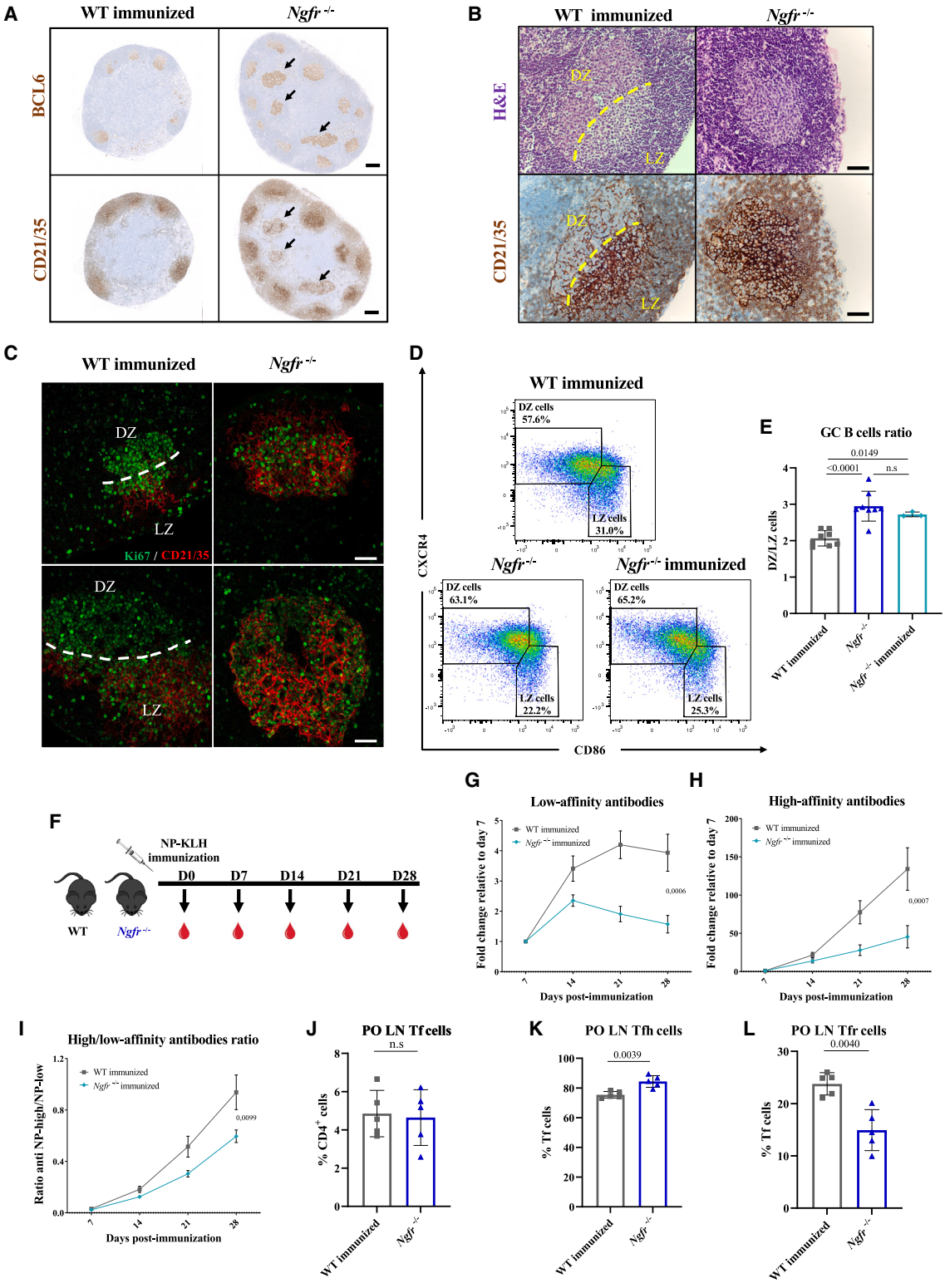


(legend on next page)

Please cite this article in press as: Hernández-Barranco et al., NGFR regulates stromal cell activation in germinal centers, Cell Reports (2024), https://doi.org/10.1016/j.celrep.2024.113705



revealed that the hyperplastic GC phenotype observed was not primarily due to *Ngfr* deletion in lymphoid cells.

Our analysis showed that NGFR was widely expressed by LECs and in different subsets of LSCs, including FRCs, MRCs, and FDCs. Although the expression of NGFR in some of these populations has already been reported,[12,39,40] its function remains largely unexplored. FDCs proved to be the LSC subset most significantly expanded in the $Ngfr^{-/-}$ LNs, consistent with the GC hyperplasia observed in these mice. Despite the progress in understanding FDC biology over recent years, there are still many aspects of their behavior that remain elusive due to their low frequency[41] and the limitations in their purification and culture.[42–45] Moreover, human FDCs have mainly been studied in pathological conditions, including lymphoid neoplasia or chronically inflamed resected tonsils.[46,47] The comparison between WT FDCs in naive and immunized mice revealed that NGFR is downregulated upon FDC activation. Furthermore, we demonstrated that NGFR is essential to restrict FDC activation in the absence of inflammation. $Ngfr^{-/-}$ FDCs spontaneously adopt an activated phenotype, similar to that described during immune responses[27] and with the modulation of genes regulating FDC maturation among LZ-FDCs.[15,27,48–55]

Tumor necrosis factor (TNF)-α and lymphotoxin (LT)-α1β2 are two non-redundant factors required for FDCs to mature from stromal precursors, both within SLOs and in ectopic tertiary lymphoid structures.[15,56,57] A few other stimuli have also been reported to contribute to FDC differentiation and function, such as retinoic acid or toll-like receptor ligands.[58,59] Notably, one of the main molecular cues regulated by TNF and LT in FDCs is the nuclear factor κB (NF-κB) pathway,[60,61] whereby the induction of I-kappa-B kinase 2 (IKK2) phosphorylation can trigger classic NF-κB signaling. This pathway promotes the upregulation of adhesion molecules in FDCs like ICAM-1 and VCAM-1, while IKK2 mutant mice fail to trigger the expression of these molecules and develop dysfunctional GCs.[15] It is worth noting that the NF-κB pathway is one of the most relevant pathways modulated by NGFR.[62] Nevertheless, in this context, it remains to be seen what is the precise mechanism by which NGFR signaling modulates FDC differentiation.

We found structural alterations in the $Ngfr^{-/-}$ GCs, with a marked loss of zonation and an aberrant distribution of the FDC network. Importantly, these alterations were also present upon immunization of $Ngfr^{-/-}$ mice, suggesting the relevance of *Ngfr* in maintaining both the architecture and functionality of the GC, even in presence of external antigens. GC zonation is a feature conserved across species,[19] suggesting it has an important role in evolution. However, the precise molecular mechanisms that drive the maturation and polarization of naive FDCs into GC FDCs are still not fully understood. Nevertheless, it is believed that the interaction between FDCs and GC B cells plays a pivotal role in this process, facilitated by chemotactic factors like CXCL12 and CXCL13.[33,63] In fact, the generation of chemotactic gradients in SLOs is crucial for the organization of these organs and ensures a correct distribution of the different cell populations.[64] Recent studies demonstrated that the mouse spleen contains a specific number of FDC clusters that serve as GC niches, which may be filled by GC B cells in response to inflammation or immunization without increasing the number of FDC clusters.[65] Our study reveals potential avenues to study the influence of NGFR and the potential role of neurotrophins in FDC polarization and positioning.

In addition, we found detectable levels of self-reactive ANAs in the serum of $Ngfr^{-/-}$ mice. There is evidence in the literature that alterations to GCs could contribute to the expansion of self-reactive clones.[22,66,67] In this context, FDCs play a dual role since they participate in the selection of high-affinity B cell clones, optimizing the exposure to external antigens and survival factors,[19,68] although they can also expose self-antigens that could contribute to the development of autoimmunity.[22,69] In our model, the frequency of Tfr cells in the GCs of $Ngfr^{-/-}$ LNs was lower to that in immunized WT mice. Hence, the reduction in Tfr cells could potentially contribute to the survival of self-reactive clones and the development of autoimmune syndromes, as reported previously.[70,71] FDCs are involved in the recruitment of Tf cells to the GCs via CXCL13 secretion,[15] and their positioning within the GC is altered when polarization is lost, affecting humoral immunity.[27] Taking into account the phenotype of $Ngfr^{-/-}$ GCs, it could be speculated that the disruptions to their structure

**Figure 5. The absence of NGFR in FDCs alters GC functionality and the B cell phenotype**

(A) Representative images of BCL6 and CD21/35 staining in PO LNs from WT immunized and $Ngfr^{-/-}$ mice. The black arrows indicate the formation of misplaced GCs. Scale bar, 200 μm.

(B) Representative H&E images (upper panels) and CD21/35 staining (lower panels) in GCs from WT immunized and $Ngfr^{-/-}$ PO LNs. The yellow dashed line divides the GC DZ and LZ. Scale bar, 50 μm.

(C) Representative images of Ki67 (green) and CD21/35 (red) staining in GCs from WT immunized and $Ngfr^{-/-}$ PO LNs. The white dashed line divides the GC DZ and LZ. Scale bar, 50 μm.

(D) Gating strategy used in the flow cytometry analysis of centroblasts (DZ B cells) and centrocytes (LZ B cells) and representative plots of these populations in WT immunized, $Ngfr^{-/-}$, and $Ngfr^{-/-}$ immunized PO LNs.

(E) Quantification of the DZ/LZ ratio based on the frequencies of centroblasts and centrocytes in WT immunized, $Ngfr^{-/-}$, and $Ngfr^{-/-}$ immunized PO LNs (n = 8 from 2 independent experiments for WT immunized and $Ngfr^{-/-}$, and n = 3 from 1 experiment for $Ngfr^{-/-}$ immunized mice).

(F) Scheme of footpad subcutaneous NP-KLH immunization and blood sampling of WT and $Ngfr^{-/-}$ mice.

(G) Fold increase in low-affinity antibodies normalized at day 7.

(H) Fold increase in high-affinity antibodies normalized at day 7.

(I) The ratio between the high- and low-affinity antibodies in the serum of WT and $Ngfr^{-/-}$ mice.

(J) Flow cytometry quantification of total Tf cells in WT immunized and $Ngfr^{-/-}$ PO LNs.

(K) Flow cytometry quantification of Tfh cells in WT immunized and $Ngfr^{-/-}$ PO LNs.

(L) Flow cytometry quantification of Tfr cells in WT immunized and $Ngfr^{-/-}$ PO LNs. (G)–(L): n = 5 from 1 experiment. In (E) and (J)–(L), the graphs show the mean and SD error bars. In (E), p values were obtained with one-way ANOVA. In (J)–(L), p values by two-tailed unpaired t test with Welch's correction. In (G)–(I), the graphs show the mean and SEM error bars and p values by two-way ANOVA.

Please cite this article in press as: Hernández-Barranco et al., NGFR regulates stromal cell activation in germinal centers, Cell Reports (2024), https://doi.org/10.1016/j.celrep.2024.113705



CellPress
OPEN ACCESS

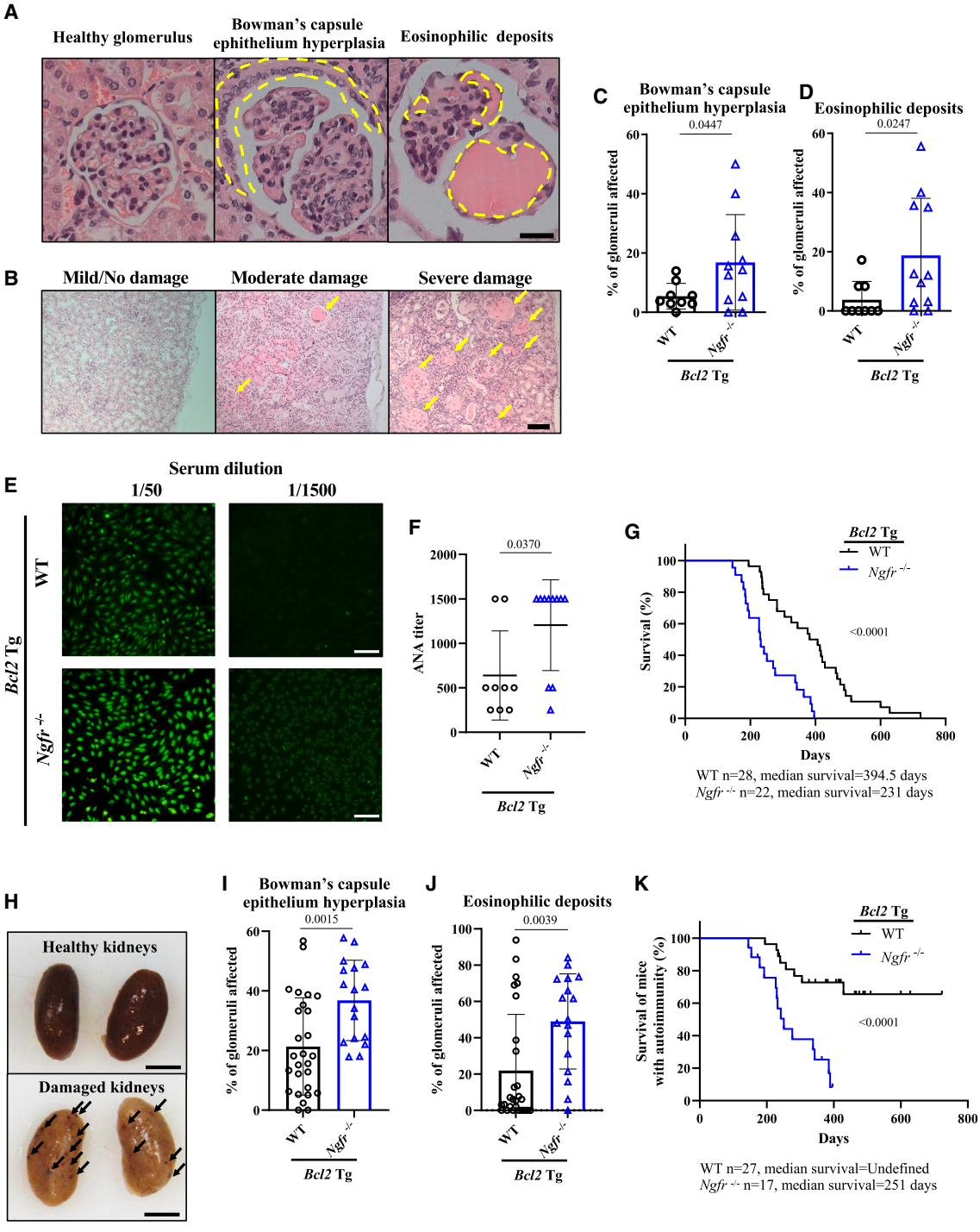


**Figure 6. *Ngfr*$^{-/-}$ decreases survival by enhancing autoimmunity in the context of BCL2 overexpression**

(A) Representative images from a healthy glomerulus (left panel) and the two markers studied to assess kidney damage (central and right panels). Scale bar, 2 μm.

(B) Representative H&E images from kidneys with mild, moderate, or severe kidney damage. Scale bar, 10 μm. The yellow arrows highlight damaged glomeruli.

(C) Quantification of the glomeruli affected by Bowman's capsule epithelium hyperplasia in the 35-week-old mouse cohorts.

(D) Quantification of the glomeruli affected by eosinophilic deposits in the 35-week-old mouse cohorts.

(E) Representative IHF images analyzing the ANAs in serum from 35-week-old *Bcl2* Tg/*Ngfr* WT and *Bcl2* Tg/*Ngfr*$^{-/-}$ mice incubated at the indicated dilutions with Hep-2 cell slides.

*(legend continued on next page)*

Please cite this article in press as: Hernández-Barranco et al., NGFR regulates stromal cell activation in germinal centers, Cell Reports (2024), https://doi.org/10.1016/j.celrep.2024.113705



may also provoke abnormal chemokine gradients, potentially affecting the populations of Tf lymphocytes. However, further data will be required to draw any conclusion.

Despite the autoantibodies detected in the serum of 10-week-old *Ngfr*$^{-/-}$ mice, we did not find any impact on autoimmunity in this mouse model. This may reflect the multistep nature of autoimmune diseases, which normally bypass sequential tolerance checkpoints prior to developing harmful manifestations.[72] Interestingly, the combination of *Ngfr*$^{-/-}$ with *Bcl2* overexpression[34] decreased OS due to a higher incidence of severe lupus-like glomerulonephritis. *Bcl2*-overexpressing mice have been used extensively to analyze autoimmune diseases *in vivo*,[35,36] and in this model, *Ngfr*$^{-/-}$ significantly increases GC formation, the FDC frequency, and the ensuing aggravation of autoantibody production. Notably, the VaV-*Bcl2* model was originally developed to replicate the progression of follicular lymphoma,[34] a chronic and incurable lymphoproliferative disease.[73,74] Our findings reveal that the shorter lifespan of *Bcl2* Tg/ *Ngfr*$^{-/-}$ mice, attributed to a higher incidence of severe autoimmune syndromes, hindered the development of high-grade follicular lymphomas. Consequently, this model has limited use in the specific study of high-grade follicular lymphomas. Importantly, increased mortality due to autoimmunity was only found in *Ngfr*$^{-/-}$ male mice, since *Bcl2* Tg/*Ngfr* WT females died significantly earlier than male mice, hindering this effect (Figure S6G). This observation could be explained due to the higher predisposition of females to autoimmunity.[75,76]

There are several studies supporting the relevance of neurotrophins signaling in autoimmune diseases, including rheumatoid arthritis, multiple sclerosis, and systemic lupus erythematosus (SLE).[77,78] While conditional deletion of the NGFR gene in B cells had beneficial effects in attenuating the symptoms of SLE in mice,[38] induction of experimental autoimmune encephalomyelitis in the same model mice as used here enhanced the severity and lethality of the disease.[79,80] These studies illustrate the complex and pleiotropic nature of NGFR and the neurotrophin signaling network, suggesting that the role of NGFR in regulating autoimmune disorders will differ in LSCs and B cells. The role of BDNF has been studied extensively in B cells, primarily characterized as a promoter of B cell survival through the activation of tropomyosin receptor kinase B (TrkB) signaling.[81–83] Moreover, it was recently demonstrated that pro-BDNF can also exacerbate autoimmunity in SLE by interacting with NGFR.[38] Conversely, how neurotrophins specifically modulate FDC physiology remains largely unexplored. Only NGFR and the high-affinity NGF receptor TrkA have been identified in FDCs, suggesting that NGF probably plays a relevant role in this stromal population.[32,84,85] In fact, adding NGF to fluorescence-activated cell sorting-isolated FDCs favors their survival in culture and the maintenance of a dendritic phenotype.[13] Exploring the interaction between these receptors and their respective ligands through different stages of the GC reaction, not only in B cells but also in FDCs, is of particular interest. There are reports providing evidence for the reciprocal inhibition of NGFR and TrkA expression depending on the context,[86] which would be consistent with evidence that the transmembrane and/or intracellular domains of NGFR interact with TrkA, facilitating conformational changes and allosteric effects that modulate the affinity and specificity of TrkA for NGF.[87] Further research is necessary to understand whether the NGFR:TrkA axis is directly involved in FDC maturation or activation. In this context, our findings show that the activation of FDCs can induce alterations in NGFR expression, suggesting that FDCs might be responsive to changes in neurotrophin levels associated with both physiological and pathological scenarios.

Collectively, our data provide evidence of the involvement of NGFR in the regulation of FDC activation and function and in preserving immune tolerance. The loss of NGFR leads to the appearance of self-reactive clones, promoting the generation of autoantibodies, which together with coexisting alterations (e.g., BCL2 overexpression) can contribute to the development of an autoimmune pathology. Our study reveals the potential origin of B cell-mediated autoimmunity, from stromal anomalies and dysregulated B cell/FDC crosstalk. These findings prompt further exploration as to whether similar anomalies may contribute to autoimmunity in patients with autoimmune-based diseases. Our data also suggest that the modulation of NGFR expression could potentially modify the severity of autoimmune syndromes. Moreover, analyzing the NGFR expression in FDCs may serve as a potential biomarker in order to monitor the progression of autoimmune disorders.

## Limitations of the study

It is important to acknowledge some limitations in our study; since we used a constitutive *Ngfr* KO model,[29] we cannot rule out whether the phenotype observed is exclusively due to the NGFR deficiency in LZ-FDCs of the *Ngfr*$^{-/-}$ mice. Further studies using conditional models to selectively deplete *Ngfr* in B cell-interacting LSC-expressing CXCL13[27] or FDC subpopulations will be crucial to clarify this issue.

Additionally, the increased mortality due to autoimmunity in *Bcl2* Tg/*Ngfr*$^{-/-}$ mice prevented us to study other GC diseases as high-grade follicular lymphoma development. As discussed above, the interpretation of the results concerning the incidence and severity of autoimmunity is also limited due to the fact that

(F) Semi-quantitative measurement of ANA titers in the sera from 35-week-old *Bcl2* Tg/*Ngfr* WT and *Bcl2* Tg/*Ngfr*$^{-/-}$ mice (C, D, and F: n = 9 *Bcl2* Tg/*Ngfr* WT; n = 11 *Bcl2* Tg/*Ngfr*$^{-/-}$ mice).

(G) Survival curve of *Bcl2* Tg/*Ngfr* WT and *Bcl2* Tg/*Ngfr*$^{-/-}$ mice.

(H) Representative image of healthy (upper panel) and damaged (lower panel) kidneys from *Bcl2* Tg mice. The black arrows denote areas of macroscopic hemorrhagic foci.

(I) Quantification of the glomeruli affected by Bowman's capsule epithelium hyperplasia in the survival cohort.

(J) Quantification of the glomeruli affected by eosinophilic deposits in the survival cohort (I and J: n = 27 *Bcl2* Tg/*Ngfr* WT, and n = 17 *Bcl2* Tg/*Ngfr*$^{-/-}$).

(K) Survival curve of *Bcl2* Tg/*Ngfr* WT and *Bcl2* Tg/*Ngfr*$^{-/-}$ mice affected by autoimmunity, i.e., with more than 20% of the glomeruli presenting signs of eosinophilic deposits. The graphs show the mean and SD error bars; p values by two-tailed unpaired t test with Welch's correction in (C) and (I), with a two-tailed Mann-Whitney test in (D), (F), and (J), and with a log rank (Mantel-Cox) test in (G) and (K).

differences in survival were only found in males. Other models of autoimmunity should be combined with *Ngfr* depletion to further understand this phenomenon.

## STAR★METHODS

Detailed methods are provided in the online version of this paper and include the following:

- KEY RESOURCES TABLE
- RESOURCE AVAILABILITY
  - Lead contact
  - Materials availability
  - Data and code availability
- EXPERIMENTAL MODEL AND STUDY PARTICIPANT DETAILS
  - Animal experiments
- METHOD DETAILS
  - Bone marrow transplantation
  - Immunization protocols
  - Assays of antibody production
  - Aging cohorts
  - ANA titration assays
  - Flow cytometry
  - Immunohistological approaches
  - Bioinformatics
- QUANTIFICATION AND STATISTICAL ANALYSIS

## SUPPLEMENTAL INFORMATION

Supplemental information can be found online at https://doi.org/10.1016/j.celrep.2024.113705.

## ACKNOWLEDGMENTS

We apologize to those authors whose work could not be cited here due to the size limitations. We thank Dr. Miguel Angel Piris, Dr. Miguel Gallardo, Dr. Verónica Matía, Dr. Maria José Jiménez Santos, and all the members of the Microenvironment and Metastasis laboratory for their help in this project.

This work was supported by project PID2020-118558RB-I00 (State Research MCIN/AEI/10.13039/501100011033), based on previous work funded by RETOS SAF2017-82924-R (MCIN/AEI/10.13039/501100011033 and cofounded by the European Regional Development fund [ERDF-EU]), and PDC2021-121102-I00 (MCIN/AEI/10.13039/501100011033, European Union "NextGenerationEU"/PRTR). We thank "la Caixa" Foundation (fellowship ID100010434, LCF/BQ/DE17/11600007) and EMBO scientific exchange grant (number 9156) awarded to A.H.-B. The CNIO, certified as a Severo Ochoa Center of Excellence, is supported by the Spanish Government through the Instituto de Salud Carlos III (ISCIII).

## AUTHOR CONTRIBUTIONS

A.H.-B. and H.P. conceived the study, designed the experiments, and interpreted the data. A.H.-B., V.S., and M. S.M. performed the majority of the experiments. L.N., F.M., S.G., A.S., and A.O.-M. performed specific experiments. E.C. performed pathological analysis of murine samples. S.L. and D.R. performed bioinformatic approaches. C.O. analyzed ANAs in murine sera. A.B., E.V., and A.D. performed the RNA-seq analysis. A.E., A.O.-M., M.C., and K.T. contributed to experimental design and interpretation. A.H.-B. prepared the figures. A.H.-B. and H.P. wrote the manuscript. H.P. supervised the study. All authors reviewed, edited, or commented on the manuscript.

## DECLARATION OF INTERESTS

The authors declare no competing interests.

Received: July 21, 2023
Revised: November 30, 2023
Accepted: January 9, 2024

## REFERENCES

1. Levi-Montalcini, R. (1952). Effects of mouse tumor transplantation on the nervous system. Ann. N. Y. Acad. Sci. *55*, 330–344.
2. Barde, Y.A., Edgar, D., and Thoenen, H. (1982). Purification of a new neurotrophic factor from mammalian brain. EMBO J. *1*, 549–553.
3. Hohn, A., Leibrock, J., Bailey, K., and Barde, Y.A. (1990). Identification and characterization of a novel member of the nerve growth factor/brain-derived neurotrophic factor family. Nature *344*, 339–341.
4. Berkemeier, L.R., Winslow, J.W., Kaplan, D.R., Nikolics, K., Goeddel, D.V., and Rosenthal, A. (1991). Neurotrophin-5: a novel neurotrophic factor that activates trk and trkB. Neuron *7*, 857–866.
5. Bothwell, M. (2016). Recent Advances in Understanding Neurotrophin Signaling*5*, p. F1000Res.
6. Chao, M.V. (1994). The p75 neurotrophin receptor. J. Neurobiol. *25*, 1373–1385.
7. Miller, F.D., and Kaplan, D.R. (1998). Life and death decisions: a biological role for the p75 neurotrophin receptor. Cell Death Differ. *5*, 343–345.
8. Bamji, S.X., Majdan, M., Pozniak, C.D., Belliveau, D.J., Aloyz, R., Kohn, J., Causing, C.G., and Miller, F.D. (1998). The p75 neurotrophin receptor mediates neuronal apoptosis and is essential for naturally occurring sympathetic neuron death. J. Cell Biol. *140*, 911–923.
9. Chao, M.V. (2003). Neurotrophins and their receptors: a convergence point for many signalling pathways. Nat. Rev. Neurosci. *4*, 299–309.
10. Schor, N.F. (2005). The p75 neurotrophin receptor in human development and disease. Prog Neurobiol *77*, 201–214.
11. Thompson, S.J., Schatteman, G.C., Gown, A.M., and Bothwell, M. (1989). A monoclonal antibody against nerve growth factor receptor. Immunohistochemical analysis of normal and neoplastic human tissue. Am. J. Clin. Pathol. *92*, 415–423.
12. Strobach, R.S., Nakamine, H., Masih, A.S., Linder, J., and Weisenburger, D.D. (1991). Nerve growth factor receptor expression on dendritic reticulum cells in follicular lymphoid proliferations. Hum. Pathol. *22*, 481–485.
13. Heesters, B.A., van Megesen, K., Tomris, I., de Vries, R.P., Magri, G., and Spits, H. (2021). Characterization of human FDCs reveals regulation of T cells and antigen presentation to B cells. JJ. Exp. Med. *218*, e20210790.
14. Parkin, J., and Cohen, B. (2001). An overview of the immune system. Lancet *357*, 1777–1789.
15. Aguzzi, A., Kranich, J., and Krautler, N.J. (2014). Follicular dendritic cells: origin, phenotype, and function in health and disease. Trends Immunol. *35*, 105–113.
16. Heesters, B.A., Myers, R.C., and Carroll, M.C. (2014). Follicular dendritic cells: dynamic antigen libraries. Nat. Rev. Immunol. *14*, 495–504.
17. Krishnamurty, A.T., and Turley, S.J. (2020). Lymph node stromal cells: cartographers of the immune system. Nat. Immunol. *21*, 369–380.
18. Victora, G.D., and Nussenzweig, M.C. (2012). Germinal centers. Annu. Rev. Immunol. *30*, 429–457.
19. Victora, G.D., and Nussenzweig, M.C. (2022). Germinal Centers. Annu. Rev. Immunol. *40*, 413–442.
20. Stebegg, M., Kumar, S.D., Silva-Cayetano, A., Fonseca, V.R., Linterman, M.A., and Graca, L. (2018). Regulation of the Germinal Center Response. Front. Immunol. *9*, 2469.

21. Mueller, S.N., and Germain, R.N. (2009). Stromal cell contributions to the homeostasis and functionality of the immune system. Nat. Rev. Immunol. *9*, 618–629.

22. Vinuesa, C.G., Sanz, I., and Cook, M.C. (2009). Dysregulation of germinal centres in autoimmune disease. Nat. Rev. Immunol. *9*, 845–857.

23. de Jong, D., and Fest, T. (2011). The microenvironment in follicular lymphoma. Best Pract. Res. Clin. Haematol. *24*, 135–146.

24. Grasso, C., Pierie, C., Mebius, R.E., and van Baarsen, L.G.M. (2021). Lymph node stromal cells: subsets and functions in health and disease. Trends Immunol. *42*, 920–936.

25. Strasser, A., Whittingham, S., Vaux, D.L., Bath, M.L., Adams, J.M., Cory, S., and Harris, A.W. (1991). Enforced BCL2 expression in B-lymphoid cells prolongs antibody responses and elicits autoimmune disease. Proc. Natl. Acad. Sci. USA *88*, 8661–8665.

26. Ersching, J., Efeyan, A., Mesin, L., Jacobsen, J.T., Pasqual, G., Grabiner, B.C., Dominguez-Sola, D., Sabatini, D.M., and Victora, G.D. (2017). Germinal Center Selection and Affinity Maturation Require Dynamic Regulation of mTORC1 Kinase. Immunity *46*, 1045–1058.e6.e1046.

27. Pikor, N.B., Mörbe, U., Lütge, M., Gil-Cruz, C., Perez-Shibayama, C., Novkovic, M., Cheng, H.W., Nombela-Arrieta, C., Nagasawa, T., Linterman, M.A., et al. (2020). Remodeling of light and dark zone follicular dendritic cells governs germinal center responses. Nat. Immunol. *21*, 649–659.

28. Allen, C.D.C., and Cyster, J.G. (2008). Follicular dendritic cell networks of primary follicles and germinal centers: phenotype and function. Semin. Immunol. *20*, 14–25.

29. Lee, K.F., Li, E., Huber, L.J., Landis, S.C., Sharpe, A.H., Chao, M.V., and Jaenisch, R. (1992). Targeted mutation of the gene encoding the low affinity NGF receptor p75 leads to deficits in the peripheral sensory nervous system. Cell *69*, 737–749.

30. Schuhmann, B., Dietrich, A., Sel, S., Hahn, C., Klingenspor, M., Lommatzsch, M., Gudermann, T., Braun, A., Renz, H., and Nockher, W.A. (2005). A role for brain-derived neurotrophic factor in B cell development. J. Neuroimmunol. *163*, 15–23.

31. McInnes, L., Healy, J., and Melville, J. (2018). UMAP: Uniform Manifold Approximation and Projection for Dimension Reduction. Preprint at arXiv, 03426, 1802. https://doi.org/10.48550/arXiv.1802.03426.

32. Rodda, L.B., Lu, E., Bennett, M.L., Sokol, C.L., Wang, X., Luther, S.A., Barres, B.A., Luster, A.D., Ye, C.J., and Cyster, J.G. (2018). Single-Cell RNA Sequencing of Lymph Node Stromal Cells Reveals Niche-Associated Heterogeneity. Immunity *48*, 1014–1028.e6.e1016.

33. Victora, G.D., Dominguez-Sola, D., Holmes, A.B., Deroubaix, S., Dalla-Favera, R., and Nussenzweig, M.C. (2012). Identification of human germinal center light and dark zone cells and their relationship to human B-cell lymphomas. Blood *120*, 2240–2248.

34. Egle, A., Harris, A.W., Bath, M.L., O'Reilly, L., and Cory, S. (2004). VavP-Bcl2 transgenic mice develop follicular lymphoma preceded by germinal center hyperplasia. Blood *103*, 2276–2283.

35. Tischner, D., Woess, C., Ottina, E., and Villunger, A. (2010). Bcl-2-regulated cell death signalling in the prevention of autoimmunity. Cell Death Dis. *1*, e48.

36. Marín-Vidalled, M.J., Bolívar, A., Zubiaga, A., and López-Hoyos, M. (2010). The combined effect of BCL-2 over-expression and E2F2 deficiency induces an autoimmune syndrome in non-susceptible mouse strain C57BL/6. Autoimmunity *43*, 111–120.

37. Vega, J.A., García-Suárez, O., Hannestad, J., Pérez-Pérez, M., and Germanà, A. (2003). Neurotrophins and the immune system. J. Anat. *203*, 1–19.

38. Shen, W.Y., Luo, C., Hurtado, P.R., Liu, X.J., Luo, R.Y., Li, H., Hu, Z.L., Xu, J.M., Coulson, E.J., Zhao, M., et al. (2022). Up-regulation of proBDNF/p75(NTR) signaling in antibody-secreting cells drives systemic lupus erythematosus. Sci. Adv. *8*, eabj2797.

39. Labouyrie, E., Parrens, M., de Mascarel, A., Bloch, B., and Merlio, J.P. (1997). Distribution of NGF receptors in normal and pathologic human lymphoid tissues. J. Neuroimmunol. *77*, 161–173.

40. Perez-Perez, M., Garcia-Suarez, O., Esteban, I., Germana, A., Farinas, I., Naves, F.J., and Vega, J.A. (2003). p75NTR in the spleen: age-dependent changes, effect of NGF and 4-methylcatechol treatment, and structural changes in p75NTR-deficient mice. Anat Rec A Discov Mol Cell Evol Biol *270*, 117–128.

41. Heesters, B.A., Van der Poel, C.E., and Carroll, M.C. (2017). Follicular Dendritic Cell Isolation and Loading of Immune Complexes. Methods Mol. Biol. *1623*, 105–112.

42. Sukumar, S., Szakal, A.K., and Tew, J.G. (2006). Isolation of functionally active murine follicular dendritic cells. J. Immunol. Methods *313*, 81–95.

43. Schaue, D., Micewicz, E.D., Ratikan, J.A., Xie, M.W., Cheng, G., and McBride, W.H. (2015). Radiation and inflammation. Semin. Radiat. Oncol. *25*, 4–10.

44. Usui, K., Honda, S.i., Yoshizawa, Y., Nakahashi-Oda, C., Tahara-Hanaoka, S., Shibuya, K., and Shibuya, A. (2012). Isolation and characterization of naive follicular dendritic cells. Mol. Immunol. *50*, 172–176.

45. Jarjour, M., Jorquera, A., Mondor, I., Wienert, S., Narang, P., Coles, M.C., Klauschen, F., and Bajénoff, M. (2014). Fate mapping reveals origin and dynamics of lymph node follicular dendritic cells. JJ. Exp. Med. *211*, 1109–1122.

46. Steiniger, B., Trabandt, M., and Barth, P.J. (2011). The follicular dendritic cell network in secondary follicles of human palatine tonsils and spleens. Histochem. Cell Biol. *135*, 327–336.

47. Mourcin, F., Verdière, L., Roulois, D., Amin, R., Lamaison, C., Sibut, V., Thamphya, B., Pangault, C., Monvoisin, C., Huet, S., et al. (2021). Follicular lymphoma triggers phenotypic and functional remodeling of the human lymphoid stromal cell landscape. Immunity *54*, 1788–1806.e7.

48. Heesters, B.A., Chatterjee, P., Kim, Y.A., Gonzalez, S.F., Kuligowski, M.P., Kirchhausen, T., and Carroll, M.C. (2013). Endocytosis and recycling of immune complexes by follicular dendritic cells enhances B cell antigen binding and activation. Immunity *38*, 1164–1175.

49. Kosco, M.H., Pflugfelder, E., and Gray, D. (1992). Follicular dendritic cell-dependent adhesion and proliferation of B cells in vitro. JJ. Immunol. *148*, 2331–2339.

50. Balogh, P., Aydar, Y., Tew, J.G., and Szakal, A.K. (2002). Appearance and phenotype of murine follicular dendritic cells expressing VCAM-1. Anat. Rec. *268*, 160–168.

51. Carrasco, Y.R., Fleire, S.J., Cameron, T., Dustin, M.L., and Batista, F.D. (2004). LFA-1/ICAM-1 interaction lowers the threshold of B cell activation by facilitating B cell adhesion and synapse formation. Immunity *20*, 589–599.

52. Duan, L., Liu, D., Chen, H., Mintz, M.A., Chou, M.Y., Kotov, D.I., Xu, Y., An, J., Laidlaw, B.J., and Cyster, J.G. (2021). Follicular dendritic cells restrict interleukin-4 availability in germinal centers and foster memory B cell generation. Immunity *54*, 2256–2272.e6.

53. Lu, E., and Cyster, J.G. (2019). G-protein coupled receptors and ligands that organize humoral immune responses. Immunol. Rev. *289*, 158–172.

54. Spillane, K.M., and Tolar, P. (2017). B cell antigen extraction is regulated by physical properties of antigen-presenting cells. J. Cell Biol. *216*, 217–230.

55. Park, C.S., Yoon, S.O., Armitage, R.J., and Choi, Y.S. (2004). Follicular dendritic cells produce IL-15 that enhances germinal center B cell proliferation in membrane-bound form. JJ. Immunol. *173*, 6676–6683.

56. Fu, Y.X., and Chaplin, D.D. (1999). Development and maturation of secondary lymphoid tissues. Annu. Rev. Immunol. *17*, 399–433.

57. Tumanov, A.V., Kuprash, D.V., and Nedospasov, S.A. (2003). The role of lymphotoxin in development and maintenance of secondary lymphoid tissues. Cytokine Growth Factor Rev. *14*, 275–288.

58. Koning, J.J., Rajaraman, A., Reijmers, R.M., Konijn, T., Pan, J., Ware, C.F., Butcher, E.C., and Mebius, R.E. (2021). Development of follicular dendritic

cells in lymph nodes depends on retinoic acid-mediated signaling. Development *148*.

59. El Shikh, M.E.M., El Sayed, R.M., Wu, Y., Szakal, A.K., and Tew, J.G. (2007). TLR4 on follicular dendritic cells: an activation pathway that promotes accessory activity. JJ. Immunol. *179*, 4444–4450.
60. Ware, C.F. (2005). Network communications: lymphotoxins, LIGHT, and TNF. Annu. Rev. Immunol. *23*, 787–819.
61. Myers, R.C., King, R.G., Carter, R.H., and Justement, L.B. (2013). Lymphotoxin alpha1beta2 expression on B cells is required for follicular dendritic cell activation during the germinal center response. Eur. J. Immunol. *43*, 348–359.
62. Reichardt, L.F. (2006). Neurotrophin-regulated signalling pathways. Philos. Trans. R. Soc. Lond. B Biol. Sci. *361*, 1545–1564.
63. Mesin, L., Ersching, J., and Victora, G.D. (2016). Germinal Center B Cell Dynamics. Immunity *45*, 471–482.
64. Lian, J., and Luster, A.D. (2015). Chemokine-guided cell positioning in the lymph node orchestrates the generation of adaptive immune responses. Curr. Opin. Cell Biol. *36*, 1–6.
65. Avancena, P., Song, T., Yao, Y., Fehlner-Peach, H., Diamond, B., Gu, H., Rajewsky, K., and Zou, Y.R. (2021). The magnitude of germinal center reactions is restricted by a fixed number of preexisting niches. Proc. Natl. Acad. Sci. USA *118*.
66. Shlomchik, M.J., Marshak-Rothstein, A., Wolfowicz, C.B., Rothstein, T.L., and Weigert, M.G. (1987). The role of clonal selection and somatic mutation in autoimmunity. Nature *328*, 805–811.
67. Shlomchik, M., Mascelli, M., Shan, H., Radic, M.Z., Pisetsky, D., Marshak-Rothstein, A., and Weigert, M. (1990). Anti-DNA antibodies from autoimmune mice arise by clonal expansion and somatic mutation. JJ. Exp. Med. *171*, 265–292.
68. Hase, H., Kanno, Y., Kojima, M., Hasegawa, K., Sakurai, D., Kojima, H., Tsuchiya, N., Tokunaga, K., Masawa, N., Azuma, M., et al. (2004). BAFF/BLyS can potentiate B-cell selection with the B-cell coreceptor complex. Blood *103*, 2257–2265.
69. Das, A., Heesters, B.A., Bialas, A., O'Flynn, J., Rifkin, I.R., Ochando, J., Mittereder, N., Carlesso, G., Herbst, R., and Carroll, M.C. (2017). Follicular Dendritic Cell Activation by TLR Ligands Promotes Autoreactive B Cell Responses. Immunity *46*, 106–119.
70. Fu, W., Liu, X., Lin, X., Feng, H., Sun, L., Li, S., Chen, H., Tang, H., Lu, L., Jin, W., and Dong, C. (2018). Deficiency in T follicular regulatory cells promotes autoimmunity. JJ. Exp. Med. *215*, 815–825.
71. Qi, J., Liu, C., Bai, Z., Li, X., and Yao, G. (2023). T follicular helper cells and T follicular regulatory cells in autoimmune diseases. Front. Immunol. *14*, 1178792.
72. Goodnow, C.C. (2007). Multistep pathogenesis of autoimmune disease. Cell *130*, 25–35.
73. Basso, K., and Dalla-Favera, R. (2015). Germinal centres and B cell lymphomagenesis. Nat. Rev. Immunol. *15*, 172–184.
74. Kahl, B.S., and Yang, D.T. (2016). Follicular lymphoma: evolving therapeutic strategies. Blood *127*, 2055–2063.
75. Angum, F., Khan, T., Kaler, J., Siddiqui, L., and Hussain, A. (2020). The Prevalence of Autoimmune Disorders in Women: A Narrative Review. Cureus *12*, e8094.
76. Kronzer, V.L., Bridges, S.L., Jr., and Davis, J.M., 3rd. (2021). Why women have more autoimmune diseases than men: An evolutionary perspective. Evol Appl *14*, 629–633.
77. Minnone, G., De Benedetti, F., and Bracci-Laudiero, L. (2017). NGF and Its Receptors in the Regulation of Inflammatory Response. Int. J. Mol. Sci. *18*, 1028.
78. Wang, N., and Tian, B. (2021). Brain-derived neurotrophic factor in autoimmune inflammatory diseases (Review). Exp. Ther. Med. *22*, 1292.
79. Küst, B., Mantingh-Otter, I., Boddeke, E., and Copray, S. (2006). Deficient p75 low-affinity neurotrophin receptor expression does alter the composition of cellular infiltrate in experimental autoimmune encephalomyelitis in C57BL/6 mice. J. Neuroimmunol. *174*, 92–100.
80. Copray, S., Küst, B., Emmer, B., Lin, M.Y., Liem, R., Amor, S., de Vries, H., Floris, S., and Boddeke, E. (2004). Deficient p75 low-affinity neurotrophin receptor expression exacerbates experimental allergic encephalomyelitis in C57/BL6 mice. J. Neuroimmunol. *148*, 41–53.
81. Schenone, A., Gill, J.S., Zacharias, D.A., and Windebank, A.J. (1996). Expression of high- and low-affinity neurotrophin receptors on human transformed B lymphocytes. J. Neuroimmunol. *64*, 141–149.
82. D'Onofrio, M., de Grazia, U., Morrone, S., Cuomo, L., Spinsanti, P., Frati, L., Gulino, A., and Ragona, G. (2000). Expression of neurotrophin receptors in normal and malignant B lymphocytes. Eur. Cytokine Netw. *11*, 283–291.
83. Fauchais, A.L., Lalloué, F., Lise, M.C., Boumediene, A., Preud'homme, J.L., Vidal, E., and Jauberteau, M.O. (2008). Role of endogenous brain-derived neurotrophic factor and sortilin in B cell survival. JJ. Immunol. *181*, 3027–3038.
84. Hannestad, J., Levanti, M.B., and Vega, J.A. (1995). Distribution of neurotrophin receptors in human palatine tonsils: an immunohistochemical study. J. Neuroimmunol. *58*, 131–137.
85. Garcia-Suarez, O., Hannestad, J., Esteban, I., Martinez del Valle, M., Naves, F.J., and Vega, J.A. (1997). Neurotrophin receptor-like protein immunoreactivity in human lymph nodes. Anat. Rec. *249*, 226–232.
86. Bredesen, D.E., and Rabizadeh, S. (1997). p75NTR and apoptosis: Trk-dependent and Trk-independent effects. Trends Neurosci. *20*, 287–290.
87. Conroy, J.N., and Coulson, E.J. (2022). High-affinity TrkA and p75 neurotrophin receptor complexes: A twisted affair. J. Biol. Chem. *298*, 101568.
88. Fletcher, A.L., Malhotra, D., Acton, S.E., Lukacs-Kornek, V., Bellemare-Pelletier, A., Curry, M., Armant, M., and Turley, S.J. (2011). Reproducible isolation of lymph node stromal cells reveals site-dependent differences in fibroblastic reticular cells. Front. Immunol. *2*, 35.
89. Schindelin, J., Arganda-Carreras, I., Frise, E., Kaynig, V., Longair, M., Pietzsch, T., Preibisch, S., Rueden, C., Saalfeld, S., Schmid, B., et al. (2012). Fiji: an open-source platform for biological-image analysis. Nat. Methods *9*, 676–682.
90. Subramanian, A., Tamayo, P., Mootha, V.K., Mukherjee, S., Ebert, B.L., Gillette, M.A., Paulovich, A., Pomeroy, S.L., Golub, T.R., Lander, E.S., and Mesirov, J.P. (2005). Gene set enrichment analysis: a knowledge-based approach for interpreting genome-wide expression profiles. Proc. Natl. Acad. Sci. USA *102*, 15545–15550.

## STAR★METHODS

### KEY RESOURCES TABLE

| REAGENT or RESOURCE | SOURCE | IDENTIFIER |
|---|---|---|
| Antibodies | | |
| FC: B220 APCeFluor780 rat monoclonal anti-mouse (clone RA3-6B2), dilution 1:200 | Thermo Fisher Scientific | Cat# 47-0452-80, RRID:AB_1518811 |
| FC: B220 BUV737 rat monoclonal anti-mouse (clone RM4-7), dilution 1:250 | BD Biosciences | Cat# 612838, RRID:AB_2870160 |
| FC: CD117 PE rat monoclonal anti-mouse (clone 2B8), dilution 1:300 | BioLegend | Cat# 105807 (also 105808), RRID:AB_313216 |
| FC: CD11b PECy7 rat monoclonal anti-mouse (clone RM4-8), dilution 1:400 | BD Biosciences | Cat# 552850, RRID:AB_394491 |
| FC: CD135 APC rat monoclonal anti-mouse (clone A2F10), dilution 1:200 | Thermo Fisher Scientific | Cat# 17-1351-82, RRID:AB_10717261 |
| FC: CD19 BV510 rat monoclonal anti-mouse (clone 1D3), dilution 1:200 | BD Biosciences | Cat# 562956, RRID:AB_2737915 |
| FC: CD21/35 BV510 rat monoclonal anti-mouse (clone 7E9), dilution 1:400 | BioLegend | Cat# 123437, RRID:AB_2876441 |
| FC: CD25 PECy7 rat monoclonal anti-mouse (clone PC61), dilution 1:300 | BD Biosciences | Cat# 561780, RRID:AB_10893596 |
| FC: CD3 BUV395 armenian hamster monoclonal anti-mouse (clone 145-2C11), dilution 1:100 | BD Biosciences | Cat# 563565, RRID:AB_2738278 |
| FC: CD31 PerCP-Cy5,5 rat monoclonal anti-mouse (clone MEC13.3), dilution 1:200 | BioLegend | Cat# 102522, RRID:AB_2566761 |
| FC: CD38AF700 rat monoclonal anti-mouse (clone 90), dilution 1:375 | Thermo Fisher Scientific | Cat# 56-0381-82, RRID:AB_657740 |
| FC: CD4 APC-Cy7 rat monoclonal anti-mouse (clone RM4-5), dilution 1:400 | BD Biosciences | Cat# 565650, RRID:AB_2739324 |
| FC: CD4 BUV395 rat monoclonal anti-mouse (clone RM4-5), dilution 1:200 | BD Biosciences | Cat# 563790, RRID:AB_2738426 |
| FC: CD45 AF700 rat monoclonal anti-mouse (clone 30-F11), dilution 1:150 | Thermo Fisher Scientific | Cat# 56-0451-82, RRID:AB_891454 |
| FC: CD45BV510 rat monoclonal anti-mouse (clone 30-F11), dilution 1:150 | BioLegend | Cat# 103138 (also 103137), RRID:AB_2563061 |
| FC: CD45.1 PercP Cy5,5 mouse monoclonal anti-mouse (clone RM4-9), dilution 1:250 | Thermo Fisher Scientific | Cat# 45-0453-82, RRID:AB_1107003 |
| FC: CD45.2 APC mouse monoclonal anti-mouse (clone RM4-10), dilution 1:250 | Thermo Fisher Scientific | Cat# 17-0454-81, RRID:AB_469399 |
| FC: CD8 PE rat monoclonal anti-mouse (clone RM4-6), dilution 1:500 | BD Biosciences | Cat# 553032, RRID:AB_394570 |
| FC: CD86 PECy7 rat monoclonal anti-mouse (clone GL1), dilution 1:100 | BioLegend | Cat# 105013 (also 105014), RRID:AB_439782 |
| FC: CD95 FITC hamster monoclonal anti-mouse (clone Jo2), dilution 1:200 | BD Biosciences | Cat# 561979, RRID:AB_10892808 |
| FC: CD95 PECy7 hamster monoclonal anti-mouse (clone Jo2), dilution 1:400 | BD Biosciences | Cat# 557653, RRID:AB_396768 |
| FC: CXCR4 PE rat monoclonal anti-mouse (clone 2B11), dilution 1:20 | Thermo Fisher Scientific | Cat# 12-9991-82, RRID:AB_891391 |
| FC: CXCR5 Biotin rat monoclonal anti-mouse (clone 2G8), dilution 1:20 | BD Biosciences | Cat# 551960, RRID:AB_394301 |

(*Continued on next page*)

Please cite this article in press as: Hernández-Barranco et al., NGFR regulates stromal cell activation in germinal centers, Cell Reports (2024), https://doi.org/10.1016/j.celrep.2024.113705





*Continued*

| REAGENT or RESOURCE | SOURCE | IDENTIFIER |
|---|---|---|
| FC: FOXP3 AF647 rat monoclonal anti-mouse (clone MF23), dilution 1/500 | BD Biosciences | Cat# 563486, RRID:AB_2738235 |
| FC: IgM PercP Cy5,5 rat monoclonal anti-mouse (clone R6-60,2), dilution 1:100 | BD Biosciences | Cat# 562034, RRID:AB_10896483 |
| FC: MAdCAM-1 APC rat monoclonal anti-mouse (clone MECA-367), dilution 1:400 | BioLegend | Cat# 120712 (also 120711), RRID:AB_2629562 |
| FC: NGFR AF488 rabbit policlonal anti-mouse, dilution 1:200 | ADVANCED TARGETING SYSTEMS | Cat# AB-N01AP-FLA, RRID:AB_3073801 |
| FC: PD1 BV421 hamster monoclonal anti-mouse (clone J43), dilution 1:100 | BD Biosciences | Cat# 565942, RRID:AB_2739406 |
| FC: Podoplanin PE syriam hamster monoclonal anti-mouse (clone eBio8.1.1), dilution 1:400 | Thermo Fisher Scientific | Cat# 12-5381-82, RRID:AB_1907439 |
| FC: Streptavidin PE, dilution 1:50 | BD Biosciences | Cat# 554061, RRID:AB_10053328 |
| FC: VCAM1 PECy7 rat monoclonal anti-mouse (clone MVCAM.A), dilution 1:400 | BioLegend | Cat# 105719 (also 105720), RRID:AB_2214047 |
| IHF: AffiniPure F(ab')2 fragment donkey anti-mouse IgG | Jackson ImmunoResearch | Cat# 715-006-151, RRID: AB_2340762 |
| IHF: chicken anti-rabbit IgG (H + L) AF647 dilution 1:750 | Thermo Fisher Scientific | Cat# A-21443, RRID:AB_2535861 |
| IHF: chicken anti-rat IgG (H + L) AF488 dilution 1:750 | Thermo Fisher Scientific | Cat# A-21470, RRID:AB_2535873 |
| IHF: donkey anti-rabbit IgG (H + L) AF488 dilution 1:750 | Thermo Fisher Scientific | Cat# A-21206 (also A21206), RRID:AB_2535792 |
| IHF: donkey anti-rabbit IgG (H + L) AF555 dilution 1:750 | Thermo Fisher Scientific | Cat# A-31572 (also A31572), RRID:AB_162543 |
| IHF: goat anti-rat IgG (H + L) AF555 dilution 1:750 | Thermo Fisher Scientific | Cat# A-21434 (also A21434), RRID:AB_2535855 |
| IHF: goat anti-rat IgG (H + L) AF647 dilution 1:750 | Thermo Fisher Scientific | Cat# A-21247, RRID:AB_141778 |
| IHF: CD21/35 APC rat monoclonal anti-mouse (clone 7E9), dilution 1:300 | BioLegend | Cat# 123412 (also 123411), RRID:AB_2085160 |
| IHF: CD21/35 unconjugated rabbit monoclonal anti-mouse (clone EP3093), dilution 1:300 | Abcam | Cat# ab75985, RRID:AB_1523292 |
| IHF: Ki67 unconjugated rabbit polyclonal anti-mouse (clone Polyclonal), dilution 1:300 | Abcam | Cat# ab15580, RRID:AB_443209 |
| IHF: MAdCAM-1 APC rat monoclonal anti-mouse (clone MECA-367), dilution 1:100 | BioLegend | Cat# 120711 (also 120712), RRID:AB_2629561 |
| IHF: NGFR unconjugated rat monoclonal anti-mouse (clone NORI146C), dilution 1:300 | Abcam | Cat# ab271290, RRID:AB_3073803 |
| IHF: VCAM1 FITC rat monoclonal anti-mouse (clone MVCAM.A), dilution 1:100 | Thermo Fisher Scientific | Cat# 11-1061-82, RRID:AB_465181 |
| IHC: BCL6 mouse monoclonal anti-mouse (clone 191E/A8), dilution 1:30 | CNIO monoclonal antibodies unit | AM (191E/A8) |
| IHC: CD21/35 rabbit monoclonal anti-mouse (clone EP3093), dilution 1:250 | Abcam | Cat# ab75985, RRID:AB_1523292 |
| IHC: CD45R/B220 rat monoclonal anti-mouse (clone RA3-3B2), dilution 1:1000 | BD Biosciences | Cat# 557390, RRID:AB_396673 |

(*Continued on next page*)

*Continued*

| REAGENT or RESOURCE | SOURCE | IDENTIFIER |
|---|---|---|
| IHC: IgG1 + IgG2a + IgG3 rabbit monoclonal anti-mouse (clone M204-3), dilution 1:500 | Abcam | Cat# ab133469, RRID:AB_2910607 |
| IHC: IgG (H + L)rabbit policlonal anti-rat, dilution 1:500 | Vector Laboratories | Cat# BA-4001, RRID:AB_10015300 |
| IHC: Ki67 rabbit monoclonal anti-mouse (clone D3B5), dilution 1:50 | Cell Signaling Technology | Cat# 12202, RRID:AB_2620142 |
| IHC: NGFR rat monoclonal anti-mouse (clone NORI146C), dilution 1:5 | CNIO monoclonal antibodies unit | AM (146C) |
| Chemicals, peptides, and recombinant proteins | | |
| 3, 30-diaminobenzidine tetrahydrochloride (Chromomap DAB Kit) | Roche | Cat# 760-159 |
| 3,3′,5,5′-Tetramethylbenzidine Liquid Substrate | Merk | Cat# T431 |
| ACK lysing buffer | Thermo Fisher Scientific | Cat# A1049201 |
| BSA | Merk | Cat# A7906 |
| Collagenase P | Roche | Cat# 11213865001 |
| DAB solution | Dako | Cat# K346811-2 |
| Dispase II | Roche | Cat# 4942078001 |
| DNase I | Roche | Cat# 4716728001 |
| EDTA | Alaos ITL | Cat# ED141C |
| Ethanol (EtOH) | ITW | Cat# 141086 |
| glycine ITW | ITW | Cat# A1067 |
| HCl | Merk | Cat# 1003142500 |
| Hematoxylin II | Dako | Cat# 790-2208 |
| Hydrogen peroxide | Dako | Cat# S202386-2 |
| Imject™ Alum | Thermo Fisher Scientific | Cat# 77161 |
| Normal donkey serum | Jackson ImmunoResearch | Cat# 017-000-121 |
| Normal goat serum | Jackson ImmunoResearch | Cat# 005-000-121 |
| NP(2,5)-BSA | Ersching J et al. ADD REF | https://www.sciencedirect.com/science/article/pii/S1074761317302339?via%3Dihub |
| NP(25)-BSA | Ersching J et al. ADD REF | https://www.sciencedirect.com/science/article/pii/S1074761317302339?via%3Dihub |
| NP-KLH (4-hydroxy-3-nitrophenyl-acetyl) hapten conjugated to Keyhole limpet hemocyanin | Biosearch technology | Cat# N-5060-5 |
| PBS | Merk | Cat# D8537 |
| PFA 16% solution EM grade | Electron Microscopy Sciences | Cat# 15710 |
| ProLong Diamond antifade mounting medium | Thermo Fisher Scientific | Cat# P36970 |
| Recombinant RNase Inhibitor | TakaraBio | Cat# 2313A |
| RPMI-1640 | Merk | Cat# R8758 |
| Single cell lysis buffer | TakaraBio | Cat# 635013 |
| Tissue-Tek O.C.T | Sakura | Cat# 4583 |
| Tissue-Tek® Glas™ Mounting Medium | Sakura | Cat# 6419 |
| Triton X-100 Sigma | Merk | Cat# T8787 |
| Tween 20 | Merk | Cat# P7949 |

(*Continued on next page*)

*Continued*

| REAGENT or RESOURCE | SOURCE | IDENTIFIER |
|---|---|---|
| **Critical commercial assays** | | |
| Agilent 2100 Bioanalyzer High Sensitivity DNA chip | Aglient | Cat# 5067-4626 |
| CD16/CD32 Mouse BD Fc Block diluted 1/50 (BD) | BD Biosciences | Cat# 553141, RRID:AB_394656 |
| eBioscience Foxp3/transcription factor Staining Buffer Set | Thermo Fisher Scientific | Cat# 00-5523-00 |
| High pH antigen retrival reagent CC1m | Roche | Cat# 950-500 |
| horseradish peroxidase (HRP) conjugated Fc-specific anti-mouse IgG1 | Jackson ImmunoResearch | Cat# 115-035-071, RRID: AB_2338506 |
| IgG AF488 (Molecular Probes) | Thermo Fisher Scientific | Cat# A-11001 (also A11001, A 11001), RRID:AB_2534069 |
| LIVE/DEAD Fixable aqua test was used as a viability dye | Thermo Fisher Scientific | Cat# L34957 |
| Low pH antigen retrival | Dako | Cat# K800521-2 |
| Nextera XT DNA library preparation kit | Illumina | Cat# FC-131-1096 |
| Novolink Polymer conjugated to HRP | Leica | Cat# RE-7161 |
| OmniMap anti-Rabbit conjugated to HRP | Roche | Cat# 760–4311, RRID:AB_2811043 |
| SMART-Seq v4 Ultra Low Input RNA Kit | TakaraBio | Cat# 634897 |
| UltraComp eBeads | Thermo Fisher Scientific | Cat# 01-2222-41 |
| **Deposited data** | | |
| Mouse reference transcriptome (mm10 v90) | NCBI | https://www.ncbi.nlm.nih.gov/datasets/genome/GCF_000001635.20/ |
| RNAseq data from WT and *Ngfr* $^{-/-}$ FDCs | This paper | GEO: GSE236511; https://www.ncbi.nlm.nih.gov/geo/query/acc.cgi?acc=GSE236511 |
| ScRNAseq data from mouse LN SCs | Rodda LB et al.[32] | GEO: GSE112903; https://www.ncbi.nlm.nih.gov/geo/query/acc.cgi?acc=GSE112903 |
| ScRNAseq data from mouse LN SCs expressing CXCL13 | Pikor NB et al.[27] | https://www.nature.com/articles/s41590-020-0672-y |
| **Software and algorithms** | | |
| Bcl2fastq v2.20.0.422 software | Illumina | https://support.illumina.com/downloads/bcl2fastq-conversion-software-v2-20.html |
| FACSDiva v.9.0 software | BD Biosciences | https://www.bdbiosciences.com/en-us/products/software/instrument-software/bd-facsdiva-software |
| Fiji software | Schindelin J et al.[89] | https://www.nature.com/articles/nmeth.2019 |
| FlowJo software v.10.8.1 | BD Biosciences | https://www.flowjo.com |
| GraphPad Prism software v9.4.0 (Dotmatics) | Dotmatics | https://www.graphpad.com/features |
| GSEA[90] | Subramanian A et al.[90] | https://www.gsea-msigdb.org/gsea/index.jsp |
| LAS X software | Leica | https://www.leica-microsystems.com/products/microscope-software/p/leica-las-x-ls/ |
| NIS-Elements software | Nikon | https://www.microscope.healthcare.nikon.com/en_EU/products/software/nis-elements |
| R software v4.1.2 | The R project | https://www.r-project.org/ |

(*Continued on next page*)

*Continued*

| REAGENT or RESOURCE | SOURCE | IDENTIFIER |
|---|---|---|
| Other | | |
| 5 mL polystyrene round-bottom cytometer tubes (Corning). | Corning | Cat# 352008 |
| 50 μm membranes CellTrics™ | Sysmex | Cat# 04-0042-2317 |
| 70 μm filters | Cultek | Cat# 45352350 |
| 96 wells round-bottom plates (Thermo Fisher Scientific) | Thermo Fisher Scientific | Cat# 143761 |
| 96-well flat bottom Nunc-Immuno™ MaxiSorp™ plates (Thermo Fisher Scientific). | Merk | Cat# 9018 |
| Automatic cell counter Countess 3 FL | Thermo Fisher Scientific | AMQAF2000 |
| Autostainer Link | Dako | N/A |
| BD FACSCanto II | BD Biosciences | N/A |
| Cryostat CM1950 | Leica | N/A |
| Hep-2 coated slides Kallestad™ | Bio-Rad | Cat# 26104 |
| HiSeq 2500 | Illumina | Cat# SY-401-2501 |
| Irrradiator Mark I 30 A | J. L. Shepherd & Associates | N/A |
| LSR Fortessa X-20 | BD Biosciences | N/A |
| Modulus™ II microplate reader | Turner BioSystems | N/A |
| Nikon Eclipse Ni-E microscope | Nikon | N/A |
| Qubit® fluorometer | Thermo Fisher Scientific | N/A |
| Superfrost ® Plus microscope slides | Thermo Fisher Scientific | Cat# J1810AMNZ |
| TCS SP5 Leica confocal microscope | Leica | N/A |
| TCS SP8 X Leica confocal microscope | Leica | N/A |
| Tissue-Tek Glass | Sakura | N/A |
| Tissue-Tek Prisma Plus | Sakura | N/A |
| Ventana Discovery XT | Roche | N/A |

## RESOURCE AVAILABILITY

### Lead contact

Further information and requests for resources and reagents should be directed to and will be fulfilled by the lead contact, Dr. Peinado hpeinado@cnio.es.

### Materials availability

Reagents described in this paper are available from the lead contact upon request with a completed Material Transfer Agreement.

### Data and code availability

(1) All data reported in this paper will be shared by the lead contact upon request.
(2) RNA sequencing data generated in this paper have been deposited to GEO under the accession number GSE236511. DOIs for other datasets analyzed here are listed in the key resources table.
(3) Any additional information required to reanalyze the data reported in this paper is available from the lead contact upon request

## EXPERIMENTAL MODEL AND STUDY PARTICIPANT DETAILS

### Animal experiments

The protocols for all the mouse experiments were approved by the Institutional Ethics Committee for Research and Animal Welfare (CEIyBA) at the CNIO (IACUC 012–2017), the Instituto de Salud Carlos III (ISCIII, CBA 17_2017v3) and the Comunidad Autónoma de Madrid (CAM, PROEX 225/17). The *Ngfr* $^{-/-}$ mice were purchased from Jackson Laboratory RRID:IMSR_JAX:002213 (https://www.jax.org/strain/002213), while the *Bcl2* Tg mice were kindly provided by Dr Suzanne Cory (Walter and Eliza Hall Institute of Medical Research, Melbourne, Australia).[34] Both models, originally generated in a C57/BL6 background, were backcrossed for up to 8 generations with WT mice on a C57BL/6JOlaHsd (Envigo, RRID:IMSR_ENV:HSD-057). For WT and *Ngfr* $^{-/-}$ models male and female

Please cite this article in press as: Hernández-Barranco et al., NGFR regulates stromal cell activation in germinal centers, Cell Reports (2024), https://doi.org/10.1016/j.celrep.2024.113705





mice were used. For *Bcl2* Tg mice, the study was restricted to male mice due to an increased autoimmune phenotype observed in *Bcl2* Tg *Ngfr* WT females (Figure S6G). The mice were bred and housed in specific pathogen-free conditions maintained on a regular 12-h light-dark cycle in a temperature-controlled room (22 ± 1°C). Unless indicated otherwise, animals between 8 and 12 weeks of age were used in the experiments. The specific procedures followed are described below.

## METHOD DETAILS

### Bone marrow transplantation

To generate BM chimeras, 5-6-week-old mice were irradiated with two doses of 4.5 Gy, separated by a 4-h interval, and 8 h after the first dose 5 x$10^6$ BM cells from donor mice were resuspended in 100 μL of PBS and infused into the irradiated animals by retro-orbital injection. BM cells were collected by flushing 4 mL of PBS into the femur and tibiae of donor mice with a 26G needle, and they were further disaggregated with a 19G needle, centrifuged and filtered through 70 μm filters (Cultek) and counted in a Neubauer chamber. Irradiated animals were sacrificed 4 weeks after BM reconstitution and LNs or blood were sampled for further analysis.

### Immunization protocols

To study GC formation in the LNs, animals were immunized by subcutaneously injecting the footpad with 10 μg of the NP (4-hydroxy-3-nitrophenyl-acetyl) hapten conjugated to Keyhole limpet hemocyanin (NP-KLH: Biosearch Technology). The NP-KLH was mixed with 10 μL of Imject Alum (Thermo Fisher Scientific) as an adjuvant and delivered in a total volume of 30 μL PBS. PO LNs were sampled at 10 days for further analysis.

### Assays of antibody production

To study the process of antibody production, animals were immunized by subcutaneously injecting NP-KLH into both footpads as described above. Blood samples were taken from the submandibular venous sinus prior to immunization, and once weekly over four weeks after immunization to characterize the antibody levels in serum. The blood samples were centrifuged for 10 min at 10,000 g, and the serum was collected and stored at −80°C. Specific anti-NP IgG1 antibodies were detected by ELISA in 96-well Clear Flat Bottom Polystyrene High Bind Microplates (Corning). The plates were incubated ON with 10 μg/mL of NP(2,5)-BSA or NP(25)-BSA as the coating reagent kindly provided by Dr Alejo Efeyan. The wells were then rinsed three times with PBS/0.04% Tween 20 (Merk) and blocked for 1 h with PBS/0.04% Tween 20 containing 2% BSA. The plates were rinsed three times with PBS/0.04% Tween 20 and incubated for 2 h with 3-fold dilutions of the serum samples, starting at a 1/250 dilution. Plates were rinsed and further incubated for 1 h with a horseradish peroxidase (HRP) conjugated Fc-specific anti-mouse IgG1 (Jackson ImmunoResearch) diluted 1/2000 in PBS/0.04% Tween 20. After a final rinse, 3,3′,5,5′-Tetramethylbenzidine Liquid Substrate (Merk) was used to develop the assay and the reaction was stopped after 1 min by adding 1M HCl. Optical density was measured at 450 nm in a Modulus II microplate reader (Turner BioSystems) and the titers were calculated by logarithmic interpolation of the dilutions, using the readings immediately above and immediately below an OD450 of 0.2 (as detailed elsewhere).[26]

### Aging cohorts

Ageing cohorts of *Ngfr* $^{-/-}$ and *Bcl2* Tg mice were established to study the long-term health of these animals, sacrificing the mice and obtaining samples when they reached the humane endpoint. In the 35-week-cohort the animals reaching the humane endpoint before that age were removed from the study.

### ANA titration assays

The detection of IgG ANAs in the serum of *Ngfr* $^{-/-}$ and *Bcl2* Tg mice was performed by IHF on Hep-2 coated slides (Kallestad Bio-Rad) according to the manufacturer's instructions. The sera were diluted 1/50, 1/250, 1/500 or 1/1500 in PBS, and a 20 μL drop was applied to the assigned antigen wells together with the controls, which were incubated for 30 min at RT in a moist chamber. The wells were rinsed, washed with PBS for 10 min and 20 μL of the conjugated anti-mouse IgG AF488 (Thermo Fisher Scientific) diluted 1/200 in PBS was added to each well. After incubation with the secondary antibodies and washing as indicated before, the sera were analyzed on a Nikon Eclipse Ni-E microscope (Nikon) using NIS-Elements software (Nikon). The ANA titers were expressed as the highest dilution showing nuclear positivity for IgG and assessed using the Mann-Whitney test.

### Flow cytometry

Single cell suspensions of LNs were obtained as described previously,[88] dissociating the LNs in 2 mL of Dispase II (0.8 mg/mL: Roche), Collagenase P (0.2 mg/mL: Roche) and DNase I (0.1 mg/mL: Roche) prepared fresh in RPMI-1640 (Merk). The tissue was incubated at 37°C in a water bath, moved gently every 5 min, and after 20 min the LNs were dissociated by pipetting. The largest fragments were allowed to settle and the soluble fraction was removed and transferred to 10 mL of ice-cold FACS buffer (PBS, 5 mM EDTA (Alaos ITL), 0.1% BSA). A further 1 mL of the digestion mix was added to the fragments for another 10 min digestion and the combined supernatant was centrifuged for 4 min at 300 g and at 4°C. The cells recovered were resuspended and filtered through 70 μm filters (Cultek). BM and blood cells were collected as described above and were then centrifuged for 4 min at 300 g and 4°C, the cell pellets were treated for 1 min with ACK lysing buffer (Thermo Fisher Scientific). This reaction was stopped

adding 10 mL of ice-cold FACS buffer and the cells were again centrifuged. The cell numbers of all the single cell suspensions were obtained in an automatic cell counter (Countess 3 FL, Thermo Fisher Scientific), and they were prepared for staining and analysis as detailed below.

For flow cytometry, the same number of cells were stained for each sample (normally 5 x $10^6$ cells), incubating single cell suspensions for 15 min at 4°C with anti CD16/CD32 Mouse BD Fc Block diluted 1/50 (BD) in 100 μL of FACS buffer in 96 wells round-bottom plates (Thermo Fisher Scientific). The cells were washed with 200 μL of FACS buffer and centrifuged for 4 min at 300 g and at 4°C. The pellets were resuspended in the antibody mix prepared for each experiment and incubated for 45 min at 4°C in the dark. The cells were washed, centrifuged again and eventually filtered through 50 μm membranes CellTrics (Sysmex) into 5 mL polystyrene round-bottom cytometer tubes (Corning).

Intracellular staining with anti-FOXP3 was achieved with the eBioscience Foxp3/transcription factor Staining Buffer Set (Thermo Fisher Scientific) according to the manufacturer instructions. The LIVE/DEAD Fixable aqua test was used as a viability dye (Thermo Fisher Scientific).

Data were acquired on BD FACSCanto II or LSR Fortessa X-20 cytometers (BD) using FACSDiva v.9.0 software (BD). Compensation was performed using UltraComp eBeads (Thermo Fisher Scientific) and the data were analyzed using FlowJo software v.10.8.1 (Tree Star).

The antibodies used for flow cytometry are detailed in the key resources table.

## Immunohistological approaches

### *Immunohistofluorescence*

For the IHF analysis, the tissues were harvested and fixed overnight (ON) in paraformaldehyde (PFA, 4% in PBS: Electron Microscopy Sciences). The tissues were then cryoprotected for 24 h in 15% and 30% sucrose solution, prior to embedding in Tissue-Tek O.C.T (Sakura) and storing at −80°C. Cryostat sections (10 μm, CM1950 Leica) were collected on Superfrost Plus microscope slides (Thermo Fisher Scientific), placed in a moist chamber, fixed with 4% PFA in PBS, and then rinsed in PBS/glycine (100 mM: ITW) and PBS/Triton X-100 (0.3%: Merk) at RT for 10 min each, washing 3 times with PBS for 5 min between each step. The tissues were blocked for 2 h in IHF buffer (PBS, 0.2% Triton X-100, 0.05% Tween 20: Merk) with 10% normal goat or donkey serum (Jackson ImmunoResearch) and 1% AffiniPure F(ab')2 fragment donkey anti-mouse IgG (Jackson ImmunoResearch). The sections were probed ON at 4°C with the primary antibodies diluted in IHF buffer (listed in the key resources table). The sections were then washed 3 times for 5 min with PBS/0.05% Tween 20 (Merk) and probed for 1 h at room temperature (RT) with secondary antibodies diluted in IHF buffer. After washing 3 more times with PBS/0.05% Tween 20 (Merk), the sections were incubated for 20 min with DAPI (5 μg/mL in PBS: Merck) and mounted in ProLong Diamond antifade mounting medium (Thermo Fisher Scientific). Images were obtained on a TCS SP5 or TCS SP8 X Leica confocal microscope using LAS X software (Leica), and the data were analyzed using Fiji software.[89] For quantification of fluorescence markers in B cell follicles (Figure 1B, 4K and 4M) up to 3 individual follicles per LN were analyzed when possible and average values were plotted.

### *Immunohistochemistry (IHC)*

For IHC, tissues were fixed ON in PBS/4% formalin and stored in 50% ethanol until they were embedded in paraffin blocks. Sections (1 μm thick) were obtained from the blocks, mounted on Superfrost Plus microscope slides (Thermo Fisher Scientific) and dried ON, before they were deparaffinized in xylene and re-hydrated through a series of graded ethanol solutions until reaching water. The tissue sections were stained with H&E using Tissue-Tek Prisma Plus (Sakura) and Tissue-Tek Glass (Sakura), or prepared for IHC in an automated immunostaining platform Ventana Discovery XT (Roche) or Autostainer Link, (Dako). Antigen retrieval was first achieved with a high pH (CC1m: Roche) or a low pH (Dako) buffer depending on the primary antibody to be used, and endogenous peroxidases were blocked with 3% hydrogen peroxide. The slides were then probed with the appropriate primary antibody (as detailed in the key resources table), which were then detected with the corresponding secondary antibodies (anti-mouse or anti-rat as needed) and visualized using OmniMap anti-Rabbit (Roche) or Novolink Polymer (Leica), conjugated to HRP when necessary. The IHC reaction was developed using either 3, 30-diaminobenzidine tetrahydrochloride (DAB, Chromomap DAB:, Roche) or a DAB solution (Dako). Hematoxylin II (Roche) was used to counterstain the nuclei prior to dehydrating, clearing and mounting the tissue in Tissue-Tek Glas Mounting Medium (Sakura). Positive control tissue sections known to express the target antigen were included in each staining run.

### *Pathological analysis of kidney damage in mice*

Histological analysis was carried out blind by the pathologist E. Caleiras (CNIO) to evaluate disease progression in the *Bcl2* Tg model. Autoimmune glomerulonephritis was defined by the presence of hypercellular and segmented glomeruli with occluded capillaries, in many cases containing eosinophilic deposits and generally accompanied by Bowman's capsule epithelium hyperplasia. The proportion of glomeruli affected by these latter alterations were quantified as a marker of severe kidney damage in 4 20x in H&E stained images of the cortical area in each mouse.

## Bioinformatics

### *RNAseq analysis*

To perform the gene expression analysis in FDCs, PO LNs from WT and *Ngfr* $^{-/-}$ mice were pooled to prepare a homogeneous cell suspension, isolating up to 300 FDCs by FACS and collecting them directly into single cell lysis buffer (TakaraBio) containing 40 U/μL

Please cite this article in press as: Hernández-Barranco et al., NGFR regulates stromal cell activation in germinal centers, Cell Reports (2024), https://doi.org/10.1016/j.celrep.2024.113705



recombinant RNase Inhibitor (TakaraBio). The cDNA obtained from the cells was amplified using the SMART-Seq v4 Ultra Low Input RNA Kit (Clontech-TakaraBio) and the amplified cDNA (1 ng) was used to generate barcoded libraries with the Nextera XT DNA library preparation kit (Illumina). The size of the libraries was checked on an Agilent 2100 Bioanalyzer High Sensitivity DNA chip and their [EMG1] concentration was determined with the Qubit fluorometer (Thermo Fisher Scientific).

The libraries were sequenced on HiSeq 2500 (Illumina) and processed with RTA v1.18.66.3. FastQ files for each sample were obtained using bcl2fastq v2.20.0.422 software (Illumina), and the sequencing reads were aligned to the mouse reference transcriptome (mm10 v90) and quantified with RSem v1.3.1. The raw counts were normalized through the TPM (Transcripts per million) and TMM (Trimmed mean of M-values) methods, transformed into log2 expression (log2(rawCount+1)), and compared to calculate the fold-change and corrected p value (false discovery rate -FDR) using a Benjamini and Hochberg procedure. Only those genes expressed with at least 1 count in a number of samples equal to the number of replicate samples of the condition with least replicates were taken into account. The RNAseq data generated have been deposited in the Gene Expression Omnibus under the accession number GSE236511. The volcano plot in Figure 4B was generated using EnhancedVolcano R package. To obtain the heatmap shown in Figure S4D, the 10 top up-regulated genes in each population of SCs were computed using the FindAllMarkers function in the Seurat R package, and they were used to represent the RNAseq expression data from *Ngfr* WT and *Ngfr* $^{-/-}$ samples. The expression data were scaled for each gene before representation. Only the genes expressed in the GSE236511 dataset are shown.

### *Comparisons with scRNAseq datasets*

Gene signature scoring was performed as described previously.[47] Briefly, scRNAseq data from mouse LN SCs were downloaded from the NCBI GEO database (GEO: GSE112903) and reanalyzed according to the original methods in Rodda LB et al.[32] or those provided elsewhere.[27] Gene signatures were obtained from *Ngfr* WT and *Ngfr* $^{-/-}$ mice, applying exclusion criteria of an FDR <0.1 and a log2 fold change (log2FC) < or > than −1 or 1. Signature scores were computed using the AddModuleScore function from the Seurat R package (v3.1.5) with R software (v4.1.2). This function calculates the average expression of each gene signature for each individual cell, subtracting the aggregate expression of the control gene sets. All the genes analyzed were separated into 25 bins based on their averaged expression and for each gene of gene signature, 100 control genes were randomly selected from the same bin as the gene. UMAPs, violin plots and heatmaps were generated using the Seurat, Vioplot (v0.3.0) and pheatmap (v1.0.12) packages, and the violin plots were analyzed using Student's t tests.

In Figure 4D, the signatures for the FDC1 cluster in the immunized and non-immunized conditions Pikor NB et al.[27] were computed with the FindMarkers function of the Seurat R package using Wilcoxon test, applying the parameters: avg_log2FC > 0.25 or < -0.25 and p_val_adj<0.05). The *Ngfr* WT and *Ngfr* $^{-/-}$ signatures were compared.

### *GSEA*

GSEA Preranked was used to perform GSEA[90] of the Reactome pathway or custom-made databases on the pre-ranked gene list of the significantly up-regulated or down-regulated genes (FDR<0.1 and FC > 1 or < -1) from the *Ngfr* WT or *Ngfr* $^{-/-}$ FDCs RNAseq described above. The settings were established for 1,000 gene set permutations, and only those gene sets with significant enrichment (FDR q value < 0.25) and more than 20 genes were finally considered.

## QUANTIFICATION AND STATISTICAL ANALYSIS

Graphs and statistical analyses were performed using GraphPad Prism software v.9.4.0 (Dotmatics), and the data are presented as the mean ± standard deviation (SD) unless otherwise indicated. All the datasets were first tested for normality using the Anderson-Darling, D'Agostino-Pearson omnibus, Shapiro-Wilk and/or Kolmogorov-Smirnov tests. The specific test used for each figure, as well as the number of biological replicates, are stated in the figure legends. Survival was represented as Kaplan-Meier curves and statistics were performed using a Log rank (Mantel-Cox) test. The p-values are indicated in each figure for statistically significant comparisons ($p < 0.05$).